

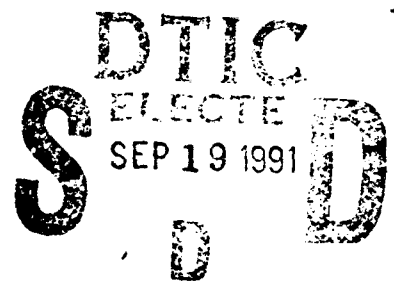
2

AD-A240 825



FINAL REPORT

**INVESTIGATION OF SURFACE BREAKDOWN ON SEMICONDUCTOR
DEVICES USING OPTICAL PROBING TECHNIQUES**



Contract No. N00014-88-K-0583

prepared by

William R. Donaldson

LABORATORY FOR LASER ENERGETICS

University of Rochester

250 East River Road

Rochester, NY 14623-1299

Telephone: 716-275-5347

E-Mail: billd@lle.rochester.edu

This document has been approved for public release and sale; its distribution is unlimited.

91-10512



I. INTRODUCTION

An extremely attractive feature of photoconductive switches is that they can be used at fairly high voltages (multikilovolts) [1,2]. The speed and high voltage handling capability of photoconductive switches is superior to that of any other device [3]. A 100-kV, 80-MW, laser-activated photoconductive power switch has been successfully operated [4]. Photoconductive switches are particularly useful for applications that require precise timing of high-voltage electrical signals with optical signals. High-power electrical pulses with picosecond rise times can be generated that are synchronous to picosecond optical pulses. The first applications of high-power, picosecond, photoconductive switching were for use in the laser fusion facility at the Laboratory for Laser Energetics (LLE) of the University of Rochester. A completely optoelectronic prepulse suppression scheme based on photoconductive switches [5] was used with LLE's OMEGA laser system. Other early applications of high-speed, high-power photoconductive switches include Pockels cells [6], Kerr cells [7], streak cameras [8], microwave pulse generation [9], and active laser mode locking [10]. An innovative linear accelerator design that utilizes ultrafast, photoconductive switching is currently under investigation at LLE [11].

Despite the utility and relative simplicity of photoconductive switches, high-voltage operation of photoconductive switches is not completely understood. A study of photoconductive switches applied to the generation of ultrafast, high-power electrical pulses is the subject of this report. The objectives of this study were: (a) to develop reliable ultrafast high-voltage photoconductive switches; (b) to develop electro-optic diagnostics for characterizing high-voltage switch operation [12]; (c) to study photoconductive switches during operation in order to obtain a better understanding of the physics of photoconductivity under high bias conditions; (d) to develop a consistent theoretical model of high-bias photoconductivity.

Statement A per telecon
Dr. Gabriel Roy ONR/Code 1132
Arlington, VA 22217-5000

NWW 9/18/91

Dist	
A-1	

II. TWO-DIMENSIONAL ELECTRO-OPTIC IMAGING SYSTEM

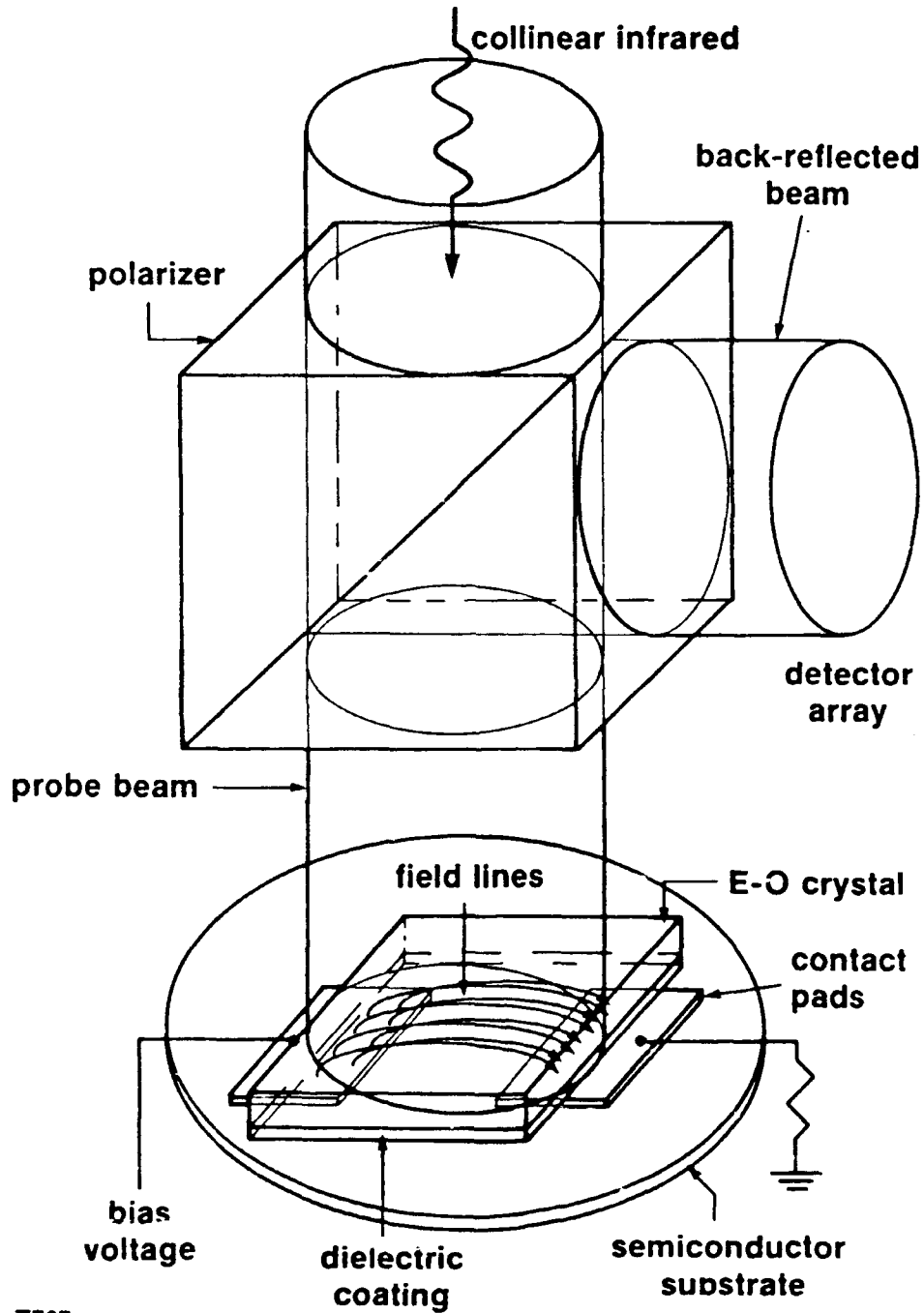
By combining electro-optic sampling, short-pulse lasers, and imaging technology, an ultrafast, 2-D, electro-optic imaging system was developed that can monitor rapid variations of the switch surface electric field over an extended region. As the tangential component of the surface field is continuous across the semiconductor interface, surface field maps can be used as a probe of the underlying carrier dynamics in the switch gap.

(A) 2-D Electro-Optic Sampling

1. System

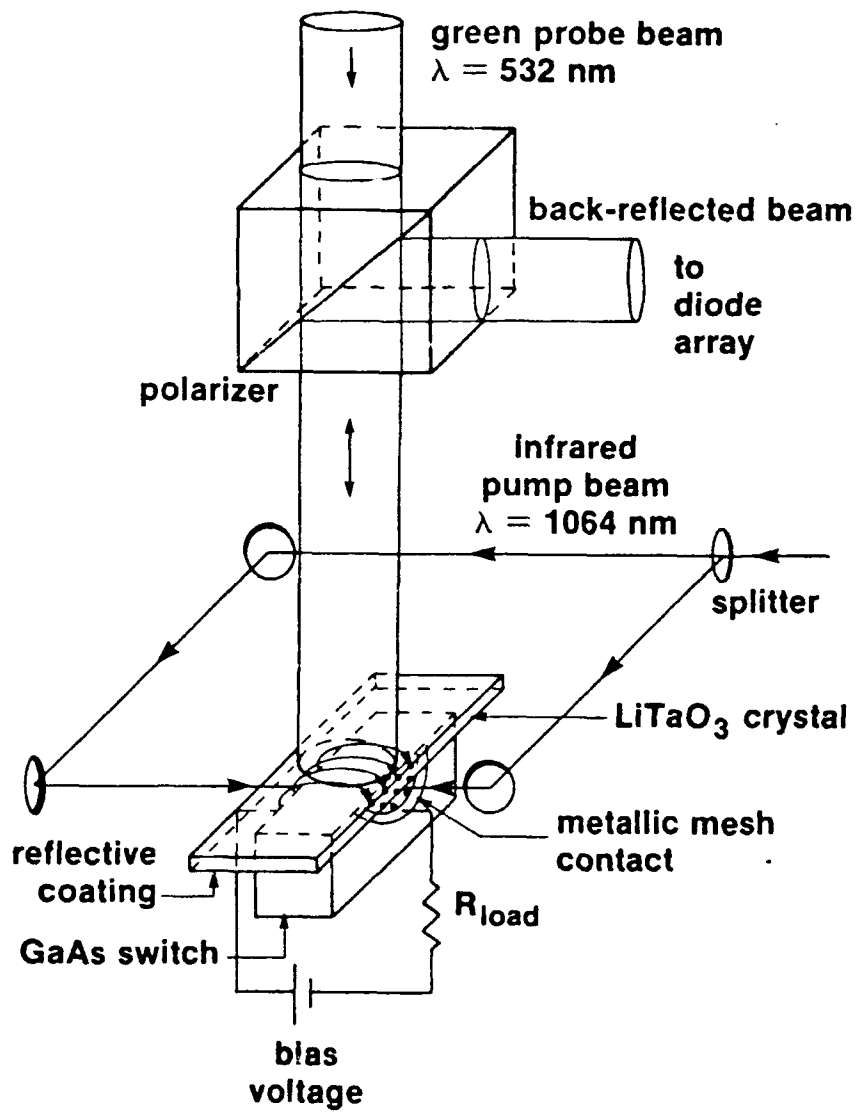
Electro-optic imaging of extended areas was made possible by using a 512×512 element video camera as the detector. With a short-pulse probe, this unique system could, in effect, obtain instantaneous "snapshots" of the surface electric field on a picosecond time scale [13,14].

Two different probe geometries were used and the pump/probe roles of the fundamental and second harmonic of Nd:YAG could be reversed. Figure 1 shows the 2-D surface field probe set up to measure the field of a photoconductive switch of a surface device type, i.e., the metallic contacts are in the same plane on the surface of a semiconductor substrate. The field was measured by placing an electro-optic crystal in the fringing field above the semiconductor surface. The crystal's birefringence changes in response to the electric field. Figure 2 shows the probe set up to measure the field of a bulk photoconductive switch, which has contacts on opposite faces of a rectangular slab of a semiconductor. The geometry shown in Fig. 2 had the advantage of a much simpler (i.e., spatially uniform) field distribution. For either type of switch, probe operation is the same, only the pump geometry is different. Each point in the beam transmitted to the detector array has sampled the local birefringence of the corresponding point in the crystal. Thus, the intensity profile of the transmitted beam is an optical replica of the electrically-induced birefringence pattern in the crystal. The back-reflected beam is imaged, through a polarizer,



Z767

Fig. 1 Detail of electro-optic probe set up to measure electric field above photoconductive switch of surface device type.



Z814

Fig. 2 Detail of electro-optic probe set up to measure electric field of GaAs bulk photoconductive switch.

onto the 2-D diode array that records the beam's intensity profile. Each pixel in the array image has a corresponding point in the crystal. The intensity at any given point in the cross section of the back-reflected beam will depend on $\sin^2\theta$, where θ is the polarization rotation experienced by that particular beam element as it traverses the crystal. The transmission to a detector element (i,j), can be written:

$$T_{ij}(V) = I_{ij}(V)/I'_{ij} = \sin^2 [(\alpha_{ij}E_{ij} + \beta_{ij})] \quad (1)$$

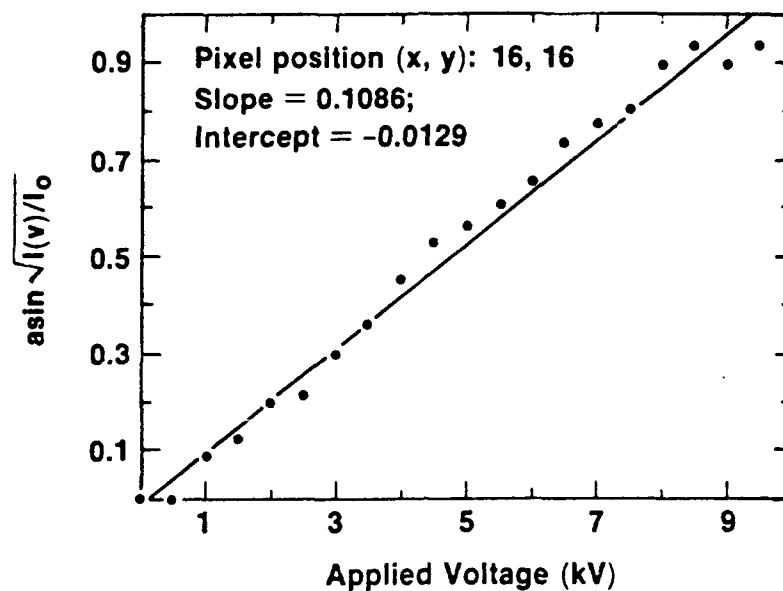
where $I_{ij}(V)$ is the light intensity measured at camera pixel (i,j) when a voltage V is applied to the electrodes; I'_{ij} is the intensity that appears at the camera if 100% of the light is imaged onto the camera without bias voltage applied; E_{ij} is the magnitude of the local electric field; α_{ij} is a constant for a given point (i,j) which relates the electro-optic coefficient to the local electric field; and β_{ij} is a constant optical rotation due to static birefringence in the crystal and $\lambda/4$ wave plate setting. The $\lambda/4$ plate setting determines where the probe beam sits on the sine-squared transmission curve with no voltage applied.

The field data must be extracted from the raw camera image. The values of α_{ij} and β_{ij} for each point (i,j) must be measured so that given the transmission T_{ij} , the field E_{ij} can be determined. The crystal is not illuminated uniformly because the probe beam has a Gaussian spatial profile. This must be considered in the analysis of the data. Therefore, *before the field can be determined, the raw image must be normalized with respect to the beam profile, so that the transmissivity and not the transmitted intensity is used.*

To calculate the transmissivity, each image acquired by the camera is normalized to a stored reference image. This reference image is the average of four frames taken with the quarter-wave plate set for maximum transmission. The light intensity is adjusted so that the most intense pixel is just within the 8-bit camera resolution; i.e., no points in the detector field are saturated. This reference image contains I'_{ij} for each point (i,j). Images normalized with respect to this reference are scaled to the maximum signal and represent $I_{ij}(V)/I'_{ij}$.

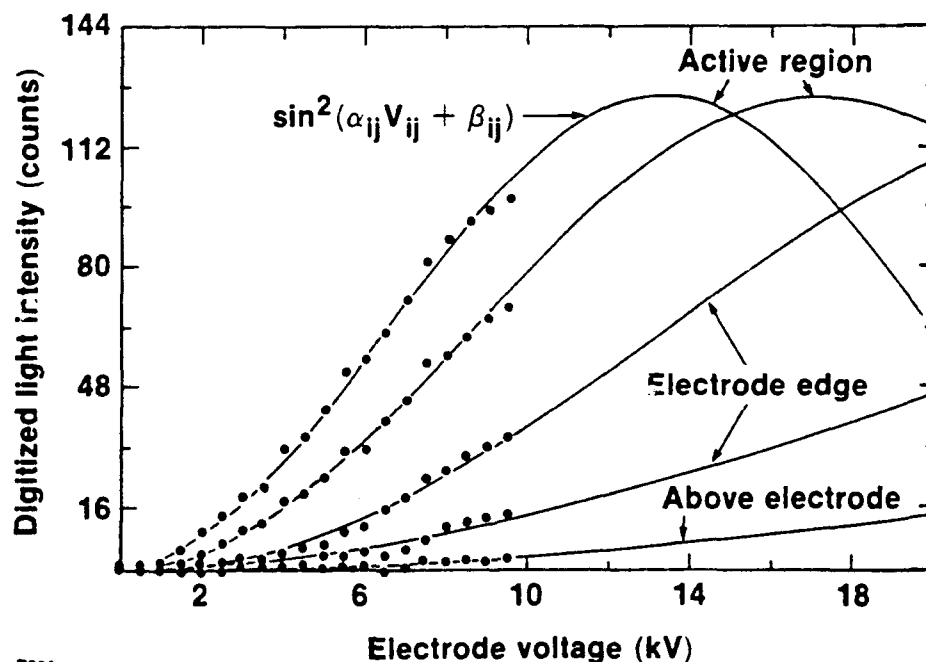
The values of α_{ij} and β_{ij} are obtained by calibrating the response of the probe to applied electric field. A quasi-dc, i.e., long compared to the light pulse, bias voltage is applied to the contacts by a computer-controlled high-voltage pulser only when an image is to be taken to eliminate any Joule heating in the switch and any thermally-induced birefringence in the e-o crystal. The bias voltage is varied from 0–9.5 kV in 500 V increments. An image was taken at each voltage. The initial data that was taken with the 2-D imaging system was reduced to a 32×32 format by averaging over pixels. This array size reduction is done so that image acquisition, processing, and display can be done with a PC rather than a workstation and in real time, i.e., without any post-processing. Later work was done with the full 512×512 images. This allows for rapid scanning of camera images. The transmission curve [Eq. (1)] for each of the elements of the reduced image was determined experimentally by this procedure. α_{ij} and β_{ij} were obtained by performing a least squares fit of the experimental transmission curve to Eq. (1) for each element in the reduced image. Figure 3 shows this dc calibration for one element of the reduced image. The biasing is chosen such that all points lie within one-half cycle of the transmission curve. Due to the sinusoidal nature of Eq. (1), it is sometimes necessary to reduce sensitivity to see large effects. The spatial variation in the crystal parameters α_{ij} and β_{ij} is illustrated in Fig. 4, which shows the calibration curves for several points in the sampling crystal.

The e-o crystal used in the 2-D work was 0.5 mm thick, y-cut LiTaO_3 . The surface switches can be studied with both the IR pump with a visible probe and the visible pump with IR probe. LiTaO_3 with different coatings was used depending on probe wavelength. The top surface of the LiTaO_3 was antireflection coated to prevent spurious back reflection and improve transmission through the crystal. The bottom surface was coated with a dielectric mirror that had a reflectivity of 99% for either the 532-nm or 1064-nm probe pulse. A conventional oscilloscope attached to the load side of the switch revealed that the green probe light caused a voltage pulse equal to about 10^{-6} times the applied bias voltage



Z805

Fig. 3 Results of DC calibration of electro-optic imaging system showing least squares fit of the experimental transmission curve to Eq. (1) for one image pixel.



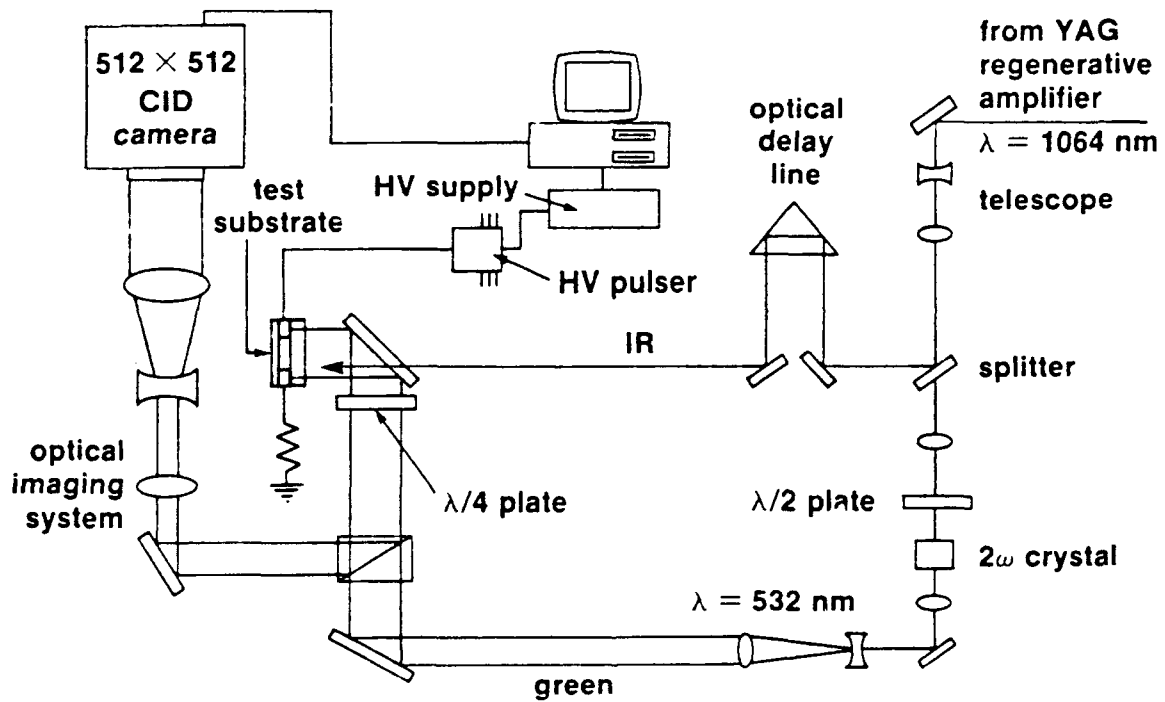
Z800

Fig. 4 Transmission function for different pixels corresponding to various positions in the e-o crystal. The active region is the area between the electrodes. Note the spatial variation in the e-o properties of the crystal, i.e., V_{π} is a function of sampled position.

to be switched to the load. This is negligible. Green or IR probes effectively do not excite the switch. The complete probe system is shown in Fig. 5

The system operation will be described for green probe light (only the relative amount of optical energy directed to the second harmonic crystal will change with probe wavelength). The infrared beam from the amplifier is first upcollimated and then split, 90% for switching use and 10% for second-harmonic generation. This green beam is upcollimated and serves as the probe beam. The green beam diameter is 1.25 cm, which completely illuminated the electrode gaps that were studied. The back-reflected green probe beam pulses are imaged onto a 512×512 element GE CID camera. The CID camera is interfaced to a personal computer through a PCVISIONplus video frame grabber supplying a digital image of the modulated probe beam. Images are digitized with 8-bit resolution. The camera response was measured to be linear with applied light intensity over the range of intensity used in this experiment. As the green probe was only 110–140 ps in duration, the switch surface field is sampled only during a short window in time. If an infrared excitation pulse illuminated the switch during this window, the switch field could be sampled during the photoconductive collapse. For surface switches, as in Fig. 1, this is accomplished by directing a pump pulse onto the switch gap collinear with the probe pulse. For the bulk switches (Fig. 2) the infrared illuminates the switch directly through the metallic mesh contacts. By sweeping the 140-ps sampling window through the photoconductively-induced event, the switch surface field can be monitored as it evolves in time. This is actually 512×512 separate, parallel pump-probe experiments, each probing a different spatial region in the electrode gap. The sampling window is moved in time by changing the length of an optical delay line in the pump beamline.

As the system operates in the high-field regime, the change in transmission to the camera is large with respect to the shot-to-shot noise in the laser pulse. Thus, the electro-optic images can be acquired with a single pulse without averaging. To ensure that the camera sees only one laser pulse, the camera and laser are synchronized to the same



Z768

Fig. 5 The complete electro-optic imaging system.

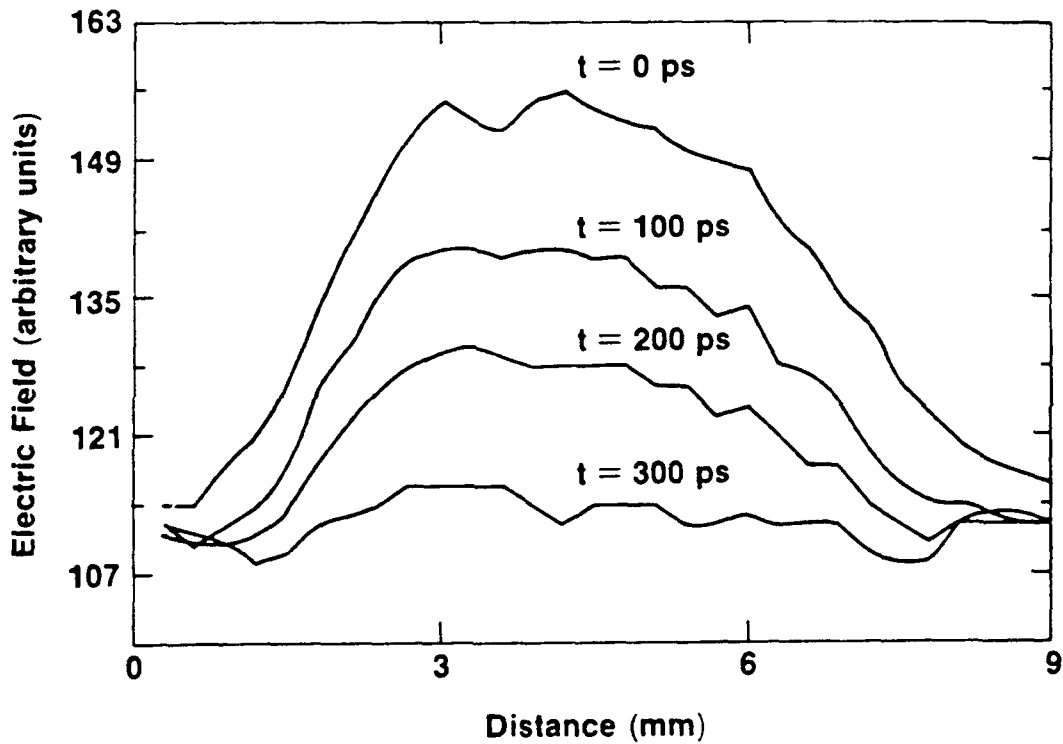
electronic oscillator, with a pulse from the camera triggering the firing of the laser. The CID camera and laser repetition rate is 30 Hz. The overall image collection rate is ~ 0.01 Hz. The overall energy of every laser pulse is measured with a fast diode. Any pulse that is not within 10% of a reference value is rejected and the measurement is repeated.

After correcting for the probe beam spatial profile and calibrating the crystal response, the surface electric field information can be decoded from the raw images from the camera. To measure the field, a frame is first acquired with high-voltage bias on and then with the bias off. The zero bias image is used to remove the contribution of the static birefringence, β_{ij} . The scaled pixel image is divided by α_{ij} , as determined by the dc calibration described earlier, to yield E_{ij} . The field, E_{ij} , is given in units of "equivalent electrode voltage," or EEV, which means that the point (i,j) is responding to the applied electric field as if a voltage E_{ij} were applied to the electrodes. Although the electrode bias voltage may be constant, the local field E_{ij} may be nonuniform due to the presence of carriers or bending of field lines due to the geometry of the electrodes. The resulting field map of the electric field has an 8-bit range and can be displayed as a false-color image on a monitor or the digital image can be manipulated to produce field contour plots, 3-D plots, or field cross sections at a particular line across the switch. The optical system is capable of producing images with a spatial resolution of $3 \mu\text{m}$ per pixel. If no pixel averaging is done, i.e., the full 512×512 image is used, the electric field can be measured with this type of spatial resolution. This requires that the above calibration procedure be applied to the entire 262,144 element array. The system will then take full images at 4 voltage settings and use that data to calculate the least squares fit. Post-processing of the full images on a Sun workstation is required to extract the electric field data. The minimum electric field sensitivity is approximately 200 V/cm and can be adjusted by rotating the quarter-wave plate before the LiTaO_3 .

(B) Imaging of Photoconductivity in Silicon

The first demonstration of the 2-D e-o imaging system was with silicon switches. The Si switches were surface devices, as in Fig. 1, where rectangular gold contact pads were deposited on a 1-in. diam., 5-mm-thick Si wafer. The electrode gap was 4 mm, and the contact width was 17 mm. The contacts were oven sintered and were measured to be ohmic to at least 1500V. A special switch holder was constructed for the multi-kilovolt bias to be used with these switches. This holder was vacuum tight, with a window for the laser pump and probe. A 50- Ω stripline, with Be-Cu spring clips, was used to connect the Si electrodes to the vacuum-tight high-voltage feedthroughs. The low side of the switch was connected by 50 Ω cable to a 50 Ω terminator. HN connectors and a coaxial RG8 cable were used. The switch holder was pumped down to ~ 1 μ m Hg and backfilled with ~ 50 psi SF₆ to prevent surface breakdown and arcing. Bias was applied with a computer-controlled 0-10 kV pulser.

Figures 6 and 7 show typical data from raw, unnormalized, uncalibrated, 32 \times 32 pixel-averaged field images obtained with the electro-optic imaging system. The LiTaO₃ crystal was 1-cm square, covering the majority of the switch gap. Figure 6 shows successive lineouts of the surface field over the 4-mm gap Si switch taken through the center of the switch parallel to the contact edge. The switch bias was 5.8 kV. Green light was used as the probe, completely illuminating the LiTaO₃ crystal. The switch gap was excited by a 150- μ J IR pump pulse. The IR pump beam had a Gaussian spatial profile and a diameter of ~ 6 mm, exciting carriers throughout the imaged region. Time is relative to the position of the IR optical delay line. The surface electric field begins collapsing at the onset of photoconductive switching and has collapsed completely within 300 ps, consistent with the ~ 200 -ps pulse width of the laser. Figure 6 illustrates the ability of the system to monitor the surface field in the switch gap during switch operation, and the ability to measure switching parameters like switch rise time, using the field across the electrode gap. The field collapse is spatially and temporally uniform for spatially uniform illumination. This is

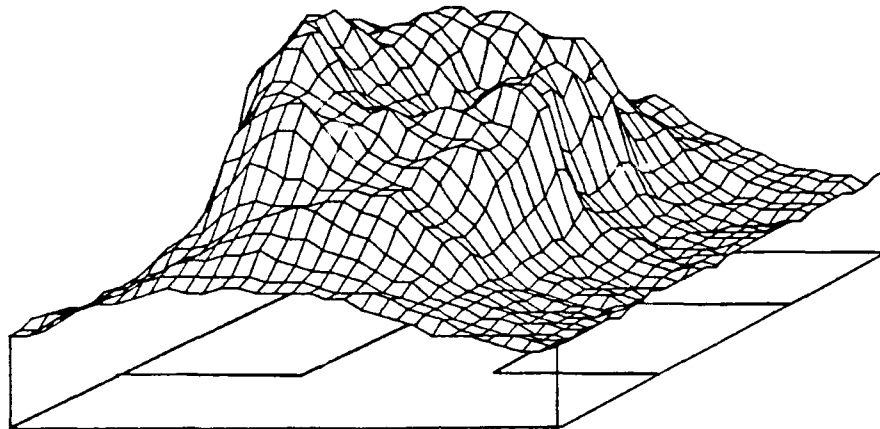


Z770

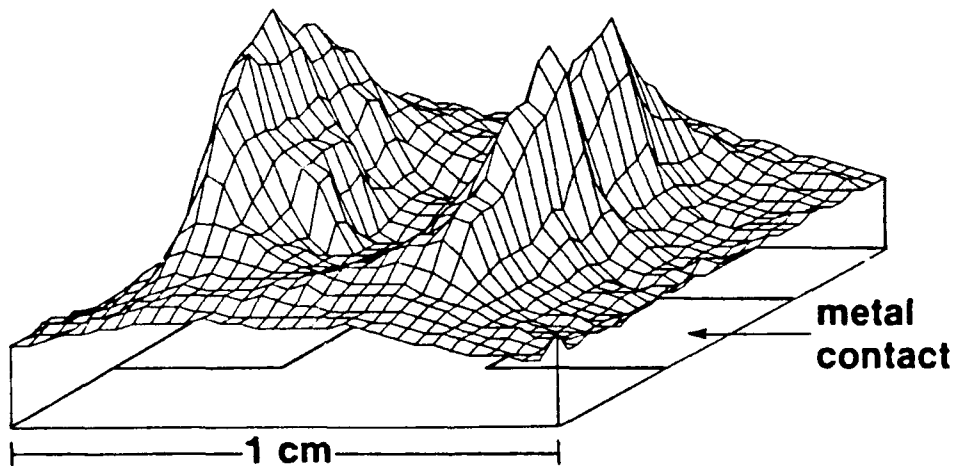
silicon substrate, 3-mm contact gap, 5.8-kV bias

Fig. 6 Collapse of electric field above IR illuminated surface type Si switch. Lineouts from raw electro-optic images taken through center of switch perpendicular to contact edge for various times (0 ps is before IR pump pulse). The switch was biased at 5.8 kV across a 4-mm contact gap. Note the spatially uniform collapse of the field. This data was taken before the imaging system development was complete and lacks later improvements in system calibration.

Before IR illumination



1 ns after IR point illumination



Z792

Fig. 7 Effect of nonuniform illumination on the electric field above Si surface type switch. Raw electro-optic images shown before and 1 ns after illumination by $40\ \mu\text{m}$ spot of IR energy at switch center. Switch was biased at 3 kV across 3-mm contact gap. Note local collapse of electric field near switch center.

typical of the imaging observed in silicon. The field collapses as the light pulse is applied and shows no oscillation or recovery (field recovery is not expected to be observed due to the μ s time scale for carrier recombination in Si). Figure 7 shows the result of nonuniform IR illumination on the Si switch surface field. The center of the switch gap was illuminated with a pinpoint ($\sim 40 \mu\text{m}$) spot of infrared laser energy. This local illumination photogenerates carriers only in a small region at the gap center. These carriers migrate outward, collapsing the surface field as they drift. Figure 7 illustrates how the system maps nonuniform fields and that carrier effects within a small region in the switch gap can be observed. One significant feature of the field on the coplanar silicon switch is that the significant field enhancements at the contact edge, suspected from the geometry, were not detected. This may be due to a number of factors including: the presence of ohmic contact, the conductivity of the substrate, and the averaging of the dielectric crystal.

After the e-o imaging system was fully operational, a more complete study of the planar Si switch was done. Switch bias was 7 kV, and the images were obtained under a pressure of ~ 50 psi SF_6 . IR probe light was used. The LiTaO_3 crystal was $1 \text{ cm} \times 3 \text{ cm}$, completely covering the $4 \text{ mm} \times 17 \text{ mm}$ switch gap.

The e-o imaging of photoconductivity in Si revealed that Si is a relatively simple photoconductive system, displaying the expected behavior. The results obtained with Si were very useful for comparison to the results obtained with GaAs switches.

III. ELECTRO-OPTIC IMAGING OF HIGH-FIELD PHOTOCONDUCTIVITY IN GAAS SWITCHES

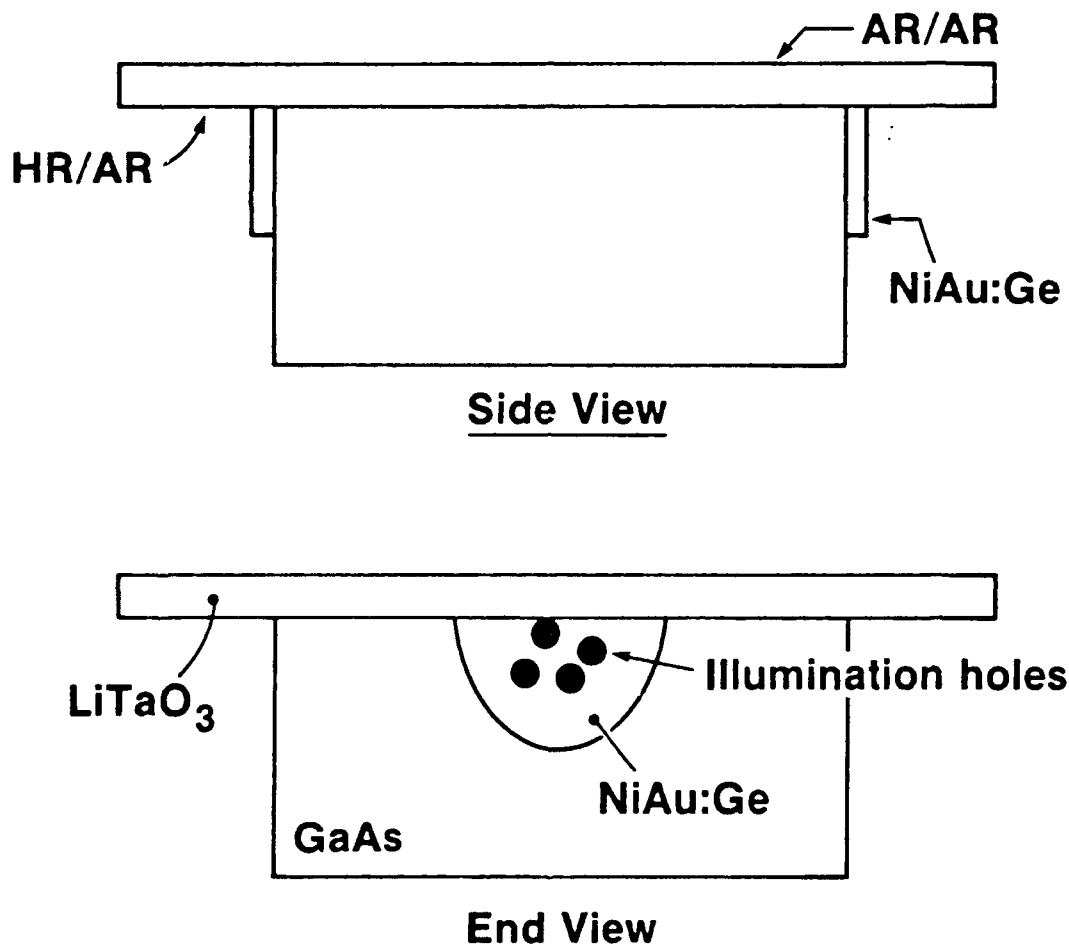
The electro-optic imaging system was used to investigate the collapse of the electric field in GaAs photoconductive switches, both bulk and planar. The motivation for this work was to provide some insight into the mechanism for observed high-field effects in GaAs switches, and to provide an experimental basis for the evaluation of a model of GaAs switch operation.

(A) Bulk Switch Operation

1. Imaging Data

Bulk switches, also called vertical switches, are switches with the electrodes on opposite sides of a slab of semiconductor. Bulk switches were prepared and their operation characterized with the e-o imaging system [15,16,17], the probe setup as in Fig. 2. These switches were fabricated by depositing circular contacts of NiAu:Ge on opposite faces of 0.6- to 1-cm-thick blocks of intrinsic GaAs. The GaAs was high resistivity material ($\rho \sim 10^7 \Omega \text{ cm}$) supplied by MA-COM. The contacts consisted of a solid annulus surrounding a center region which was perforated with holes to allow light to pass through into the bulk of the GaAs. This resulted in a nonuniform carrier density profile that decreased exponentially through the bulk of the switch. The contact preparation was also varied with the 6-mm-thick switches having an ion implantation under the metalization to make ohmic contacts, the other samples having contacts deposited on bare GaAs. This switch design is of particular interest both for its applicability to the coaxial geometry [18] and for its relative immunity to surface breakdown, as a surface arc must travel out to the edge, down the side and back into the center—a very long physical path. The design is also useful in that this contact geometry allows for uniform fields which facilitate extraction of absolute field values, as opposed to the coplanar geometry which has a much more complicated field pattern. To access the fields between the contacts, this design has been modified by cutting the GaAs in a plane passing through the center of the contacts. The switch electrode configuration is shown in detail in Fig. 8. These switches were obtained from the U.S. Army Electronics Technology and Device Laboratory.

Connection to the external circuit was made by pressure contacting copper electrodes coated with indium along the outside circumference of the NiAu:Ge electrodes. The Cu electrodes were bored out so that IR light could reach the switch contacts. By placing a dielectric beam splitter in the IR pump beam, approximately 50% of the IR light could be directed onto each electrode. Either of these beams could be blocked to investigate



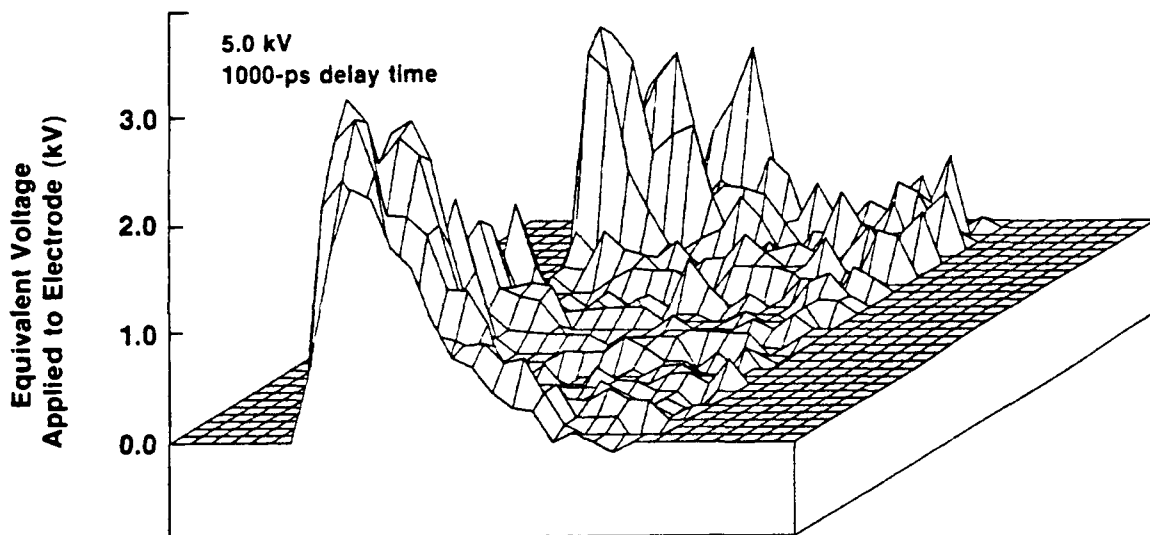
Z912

Fig. 8 Bulk GaAs switch with mesh electrodes on opposite faces. The switch has been halved and a LiTaO₃ crystal is in place to measure the surface electric field between the contacts. The LiTaO₃ crystal has an anti-reflection (AR) coating for both 532 nm and 1064 nm light on the top surface. The bottom surface has a high-reflection (HR) coating for 532 nm and an AR coating for 1064 nm.

asymmetries in the response of the photoconductor. The arrival times of the two beams at the switch were adjusted so they were coincident. The dielectric beam splitter was mounted on a kinematic mount so that it could be removed and the full IR laser energy could be applied to one side of the switch. Thus, five illumination schemes were employed, considering that full energy could be applied to either the ground or high-voltage contact.

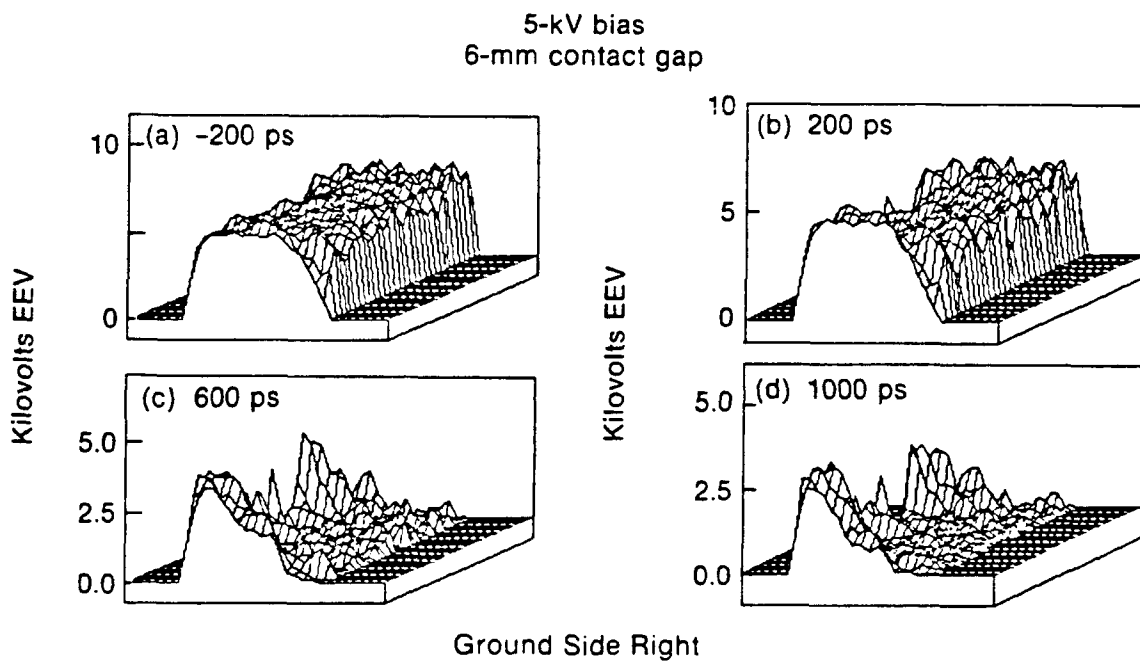
The bulk switches were mounted in a 50Ω coaxial transmission line geometry using RG8 cable. Bias voltage was applied with a computer controlled 0–9.5 kV pulser. The switch was connected via the RG8 cable to a 50Ω termination. The optical pulse width was ~200 ps for the bulk switch experiments.

Figures 9–11 show data taken for a 6-mm-thick, ion-implanted GaAs bulk switch. The images taken were normalized and scaled to equivalent electrode voltage (EEV). The true field is EEV divided by the gap distance (in this case, 6 mm). A typical e-o image is shown in Fig. 9, which shows a 3-D plot of the surface field on the 6-mm GaAs switch illuminated simultaneously through both contacts, 800 ps after initial illumination. Each contact received ~50 μJ of optical energy for a pump intensity of $1.9 \text{ mJ}/\text{cm}^2$. The left edge of the image corresponds to the negative high-voltage contact, and the right side to the ground contact. The active area in the center is 6 mm wide, and the front and back edges of the image are 10 mm apart and correspond to the edges of the deposited electrodes. Outside the region between the contacts, the field falls abruptly to zero because there is no tangential component of the electric field at the surface of a conductor. Noise spikes in that region of the image have been artificially suppressed. Initially, the image was uniform between the contacts. The infrared light has caused the field to collapse. The center section of the image is where the 2-mm-wide pump beam illuminated the GaAs. Note that the field has collapsed over most of the active region to a value of ~0.3 kV EEV although the bias voltage is 5 kV. The field collapses uniformly on the ground side of the image but it has areas of significant enhancement on the high-voltage side. There are two significant high-voltage spikes of ~3 kV EEV even though most of the switch field has collapsed. These spikes are located at



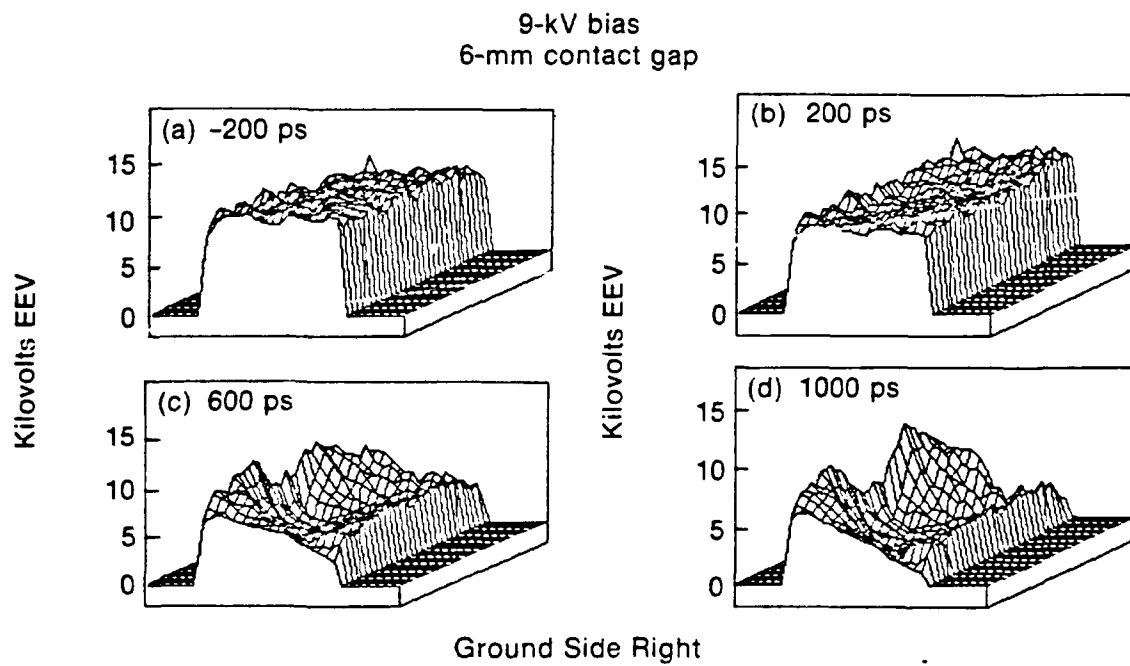
Z809

Fig. 9 The electro-optic image of the surface electric field on a GaAs switch 800 ps after illumination by a 200-ps IR pulse through both of its electrodes. The left side of the image corresponds to negative high voltage electrode. The active area is 6 mm \times 10 mm and the field enhancements are located behind the solid portion of the high voltage contact.



Z831

Fig. 10 Temporal evolution of electric field above 6-mm-thick bulk GaAs switch illuminated by 200-ps IR pulse through both contacts. Switch biased at 5 kV. Images processed and scaled to equivalent electrode voltage (EEV). The active area of the image is 6 mm \times 1 cm. The collapse of electro-optic field proceeds from the essentially uniform profile shown in (a).



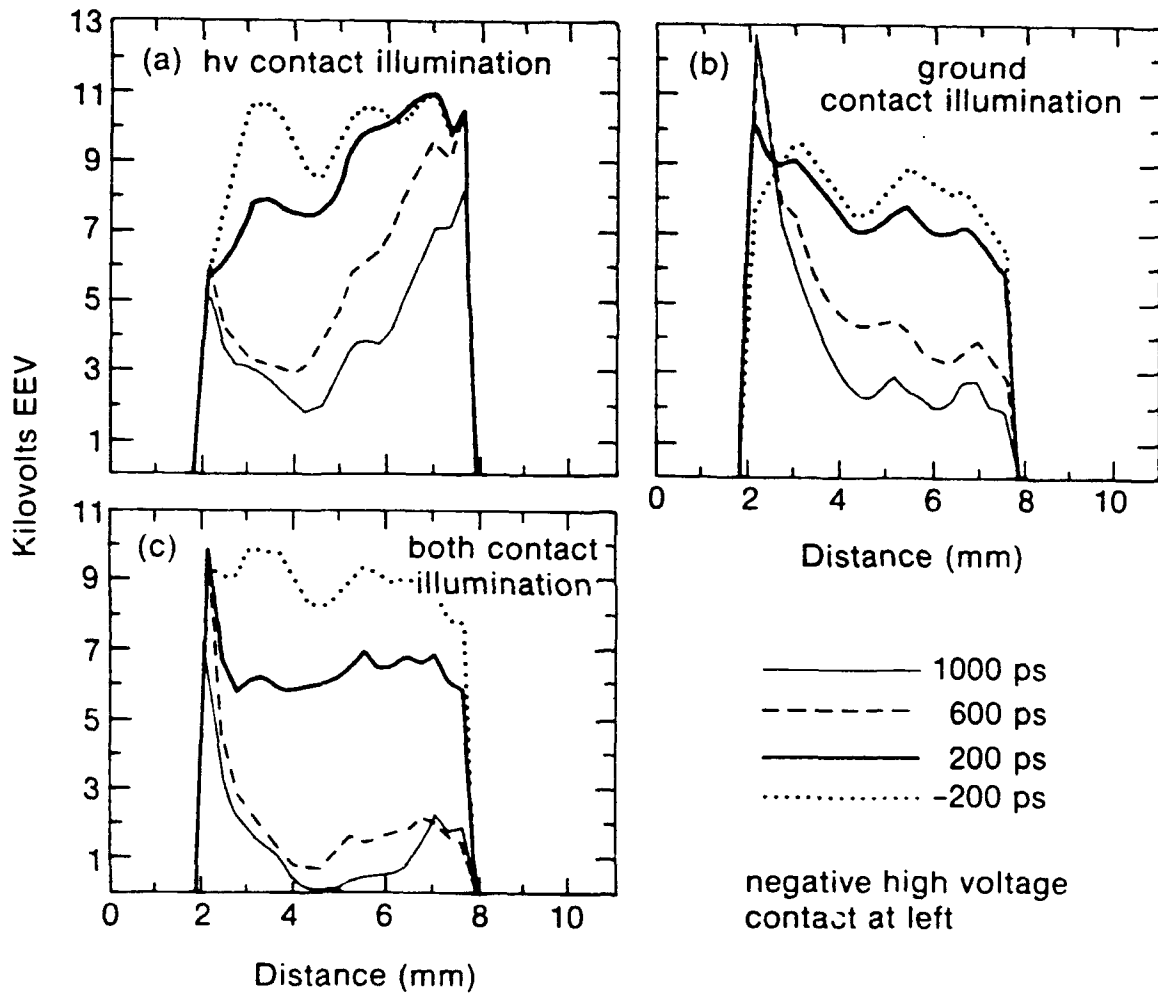
Z830

Fig. 11 Same conditions as in Fig. 10 except switch biased at 9 kV. The incomplete collapse of field is evidenced by ~ 5 kV/cm field remaining across switch after 1000 ps.

the very edges of the high-voltage contact. A survey of all the images that have been acquired reveals that this is a general feature independent of the contact preparation. There is always an enhancement at the high-voltage contact. The enhancement can be alleviated at the perforated region of the contact by illuminating with more IR light, but the field collapse is never as complete as on the ground side.

Figures 10 and 11 show a series of 3-D plots of the field above a 6-mm GaAs switch. These illustrate the progressive collapse of the surface field in time for two different bias voltages. Both contacts were illuminated simultaneously with $\sim 50 \mu\text{J}$ of IR. In Fig. 10, the switch bias was 5 kV; in Fig. 11, 9 kV. The field is given in EEV. The time is relative to the IR translation stage position; 0 ps is the arrival of the IR pulse and the stage can scan out to 1 ns after IR illumination begins. At -200 ps, the field across the switch is essentially uniform, as expected. As time progresses, the field collapses. For 5 kV bias, the collapse is almost complete, except for the enhancement near the contacts. At 9 kV, the situation is much different: the field collapses only to ~ 3 kV EEV; there is still a field of ~ 5 kV/cm across the switch, 1 ns after illumination.

Figure 12 shows a series of lineouts from the surface field images of the 6 mm GaAs switch, taken through the center of the image, perpendicular to the contact faces. These illustrate the progressive collapse of the surface field in time for various illumination schemes. Switch bias was 8 kV. Single-side illumination is characterized by a wave front that propagates across the switch. In Figs. 12(a) and 12(b), the field collapses from the illuminated contact to the nonilluminated contact in time as the region of conduction propagates from the region of photogeneration. For both-side illumination, Fig. 12(c), the field collapses more quickly and to a lower final value than for single-side illumination, as in Figs. 12(a) and 12(b). Switch rise time is faster and the efficiency is higher for illumination through both contacts, an important engineering consideration. The field enhancement exhibited in Figs. 9, 10 and 11 can also be observed in these lineouts. Small



Z834

Fig. 12 Temporal evolution of electric field above 6-mm thick bulk GaAs switch for different illumination conditions. Switch biased at 8 kV. Lineouts taken through center of processed electro-optic image at different times after illumination with 200 ps IR pulse. Greater efficiency and speed are obtained for illumination through both contacts.

differences in the -200 ps lineouts may be due to the small prepulses which excite the switch before the main IR pulse arrives, as well as the laser intensity fluctuation (~10%).

Some of these observations can be made more quantitative by defining an electro-optic switching efficiency. A standard measure of switching efficiency would be what fraction of the quasi-dc bias is switched to the load. A perfectly efficient switch would be driven completely conductive and the bias voltage would appear across the load. No electric field would remain across the switch electrodes. If the electric field across the switch is imaged electro-optically, an electro-optic switching efficiency, η , can be defined:

$$\eta = \frac{\sum_{ij} \eta_{ij}}{N} = \frac{1}{N} \sum_{ij} (E'_{ij} - E_{ij}(t)/E'_{ij}) \quad (2)$$

where the summation is over the total number of active pixels (pixels outside the electrode gap have been ignored). E'_{ij} is the electro-optic image element with no IR light present and $E_{ij}(t)$ is the electro-optic image element at a time delay t . The restrictions on the summation are that if

$$E'_{ij} - E_{ij}(t) < 0 \quad (3)$$

corresponding to a field enhancement, η , was set equal to zero (i.e., it was considered to be an element that had not undergone switching) and if

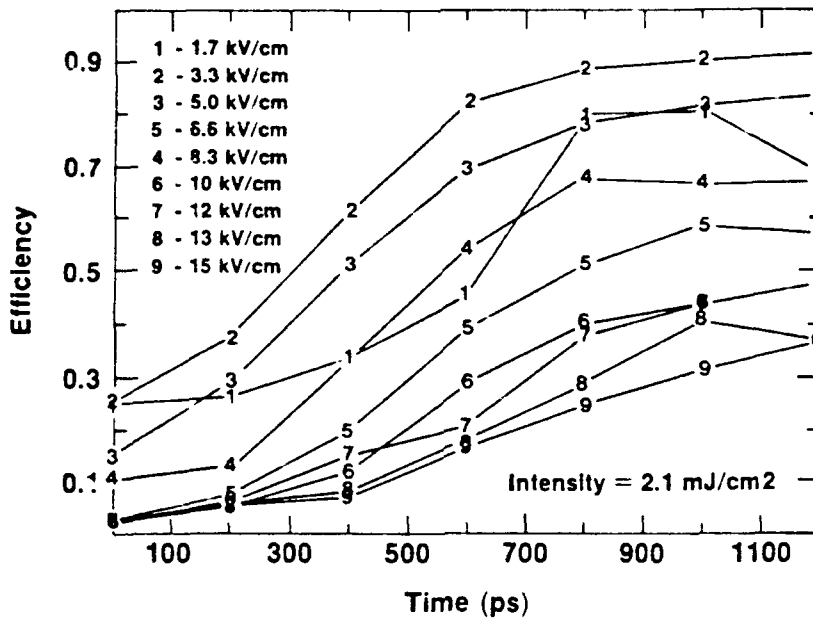
$$E'_{ij} - E_{ij}(t) > E'_{ij} \quad (4)$$

implying a negative oscillation in the surface electric field, the efficiency at that point, η , was set equal to one. The parameter η is a measure of how much of the dc surface field has been switched, and would equal the real switch efficiency if it were possible to integrate through the entire switch volume. This is impossible for these experiments. The quantity η_1 tells us what is happening at only one plane of a three-dimensional device, but is the best available measure of the internal dynamics of the switch. Figure 13 shows the electro-optic efficiency as a function of the optical delay line setting for several applied fields in the case

of two-sided illumination. The most striking feature of this graph is that the switching efficiency drops as the field increases. Figure 14 shows that this trend continues with single-side illumination at two different IR intensities. For example, at an illumination intensity of 2.1 mJ/cm^2 , there is sufficient light to switch a field of 6.6 kV/cm with 90% efficiency. At the same intensity, a field of 15 kV/cm is switched with only 40% efficiency. Figure 14(a) shows that increasing the intensity to 3.8 mJ/cm^2 increases the efficiency to only 50% at 15 kV/cm . The rise time of the switch also decreases as the light intensity is increased.

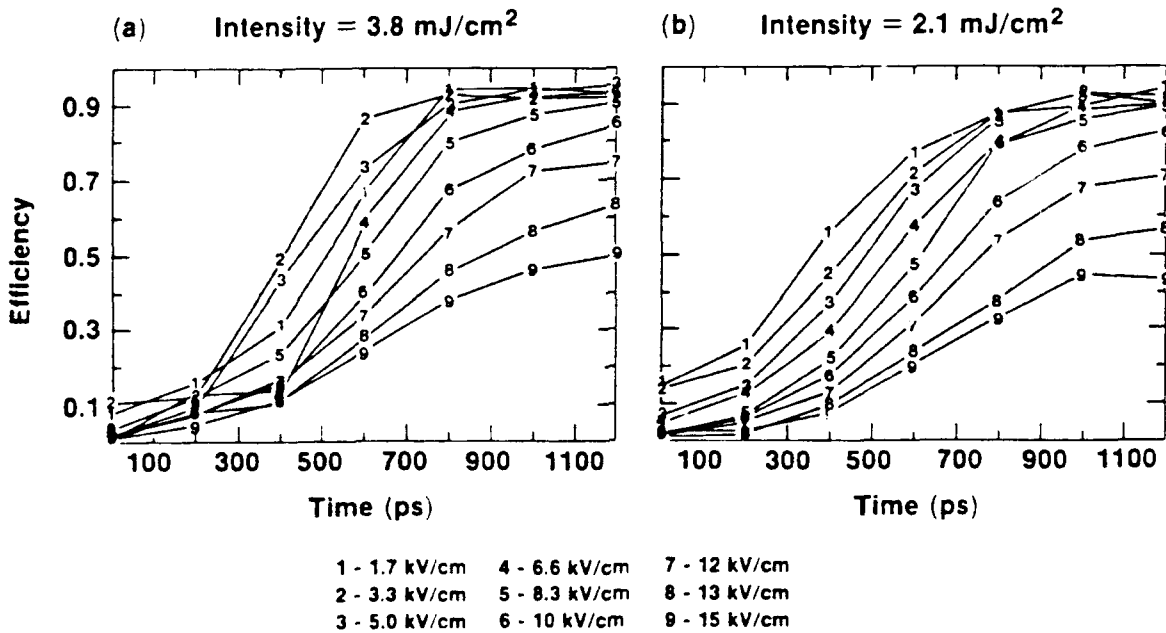
2. Discussion of Bulk Switch Data

A number of important features about how GaAs photoconductive switches operate can be discerned from this work. The first is that the electric field is enhanced at the negative high voltage electrode and collapses most slowly there. This type of behavior was seen in both types of contacts tested. In particular, the enhancement was strongest under the solid portion of the high voltage contact. A corresponding enhancement was not observed on the ground side electrode (positive with respect to the high-voltage pulse). This enhancement was reduced in the perforated region by increasing the light incident on the high voltage contact and was seen in all samples; it showed some increase with the numbers of shots applied to the sample. Thus, some of the nonuniform enhancement is associated with the long term degradation of the contact ($>2 \times 10^4$ laser shots) due to arcing from the perforated region to the solid region of the Ni: AuGe contact. This arcing only occurred if the GaAs was switched. These observed field enhancements are consistent with our simulations of bulk switches with through-the-contact illumination. Based on our simulations of the effects of non-ohmic contacts on bulk switch operation, we conclude that the persistent field enhancement at the cathode was due, in part, to the fact that the mesh electrode had alternating areas of ohmic and current-blocking contacts.



Z808

Fig. 13 The electro-optic efficiency for a 6 mm bulk GaAs photoconductive switch illuminated through both contacts as a function of time. The efficiency decreased with increasing field.



Z806

Fig. 14 The electro-optic efficiency of a GaAs photoconductive switch illuminated through only the high voltage contact; (a) 3.8 mJ/cm^2 (b) 2.1 mJ/cm^2 .

It was seen that the switching efficiency of GaAs decreased with increasing voltage out to a time ~ 1 ns after illumination. Increasing the number of carriers by increasing the IR illumination energy by a factor of ~ 2 does not significantly improve the electro-optic switching efficiency. This suggests that this is predominantly a field effect and not due to the illumination scheme. This is confirmed by the observation that, for a given bias voltage, the switching efficiency increases with increasing electrode spacing. The switching efficiency should not be a function of the bias voltage if the mobility is not a function of field. For a switch mounted in a transmission line geometry, the voltage switched to the load, V_L , is given by:

$$V_L = \frac{Z}{2Z + r} V_{BIAS} \quad (5)$$

where r is the switch resistance, V_{BIAS} is the bias voltage, and Z is the impedance of the matched bias and load cables (50Ω). The switch resistance, r , is given by

$$r = \frac{\text{voltage across switch}}{\text{switch current}} = \frac{E\ell}{JA} \quad (6)$$

where J is the total current density, ℓ is the electrode gap spacing, and A is the illuminated area of the contact. J can be written $J = ne\mu E$, with n = the density of photogenerated carriers, e is the electronic charge, and μ is the sum of carrier mobility for bipolar conduction carrier mobility. The electrical switching efficiency, V_L / V_{BIAS} , is then:

$$\frac{V_L}{V_{BIAS}} = \frac{Z}{2Z + \frac{\ell}{Ane\mu}} \quad (7)$$

There is no explicit field dependence in Eq. (7). Field dependence can only enter through the mobility, μ . Equation (7) can be verified by measuring the current at the load, I_L , versus bias voltage. Since

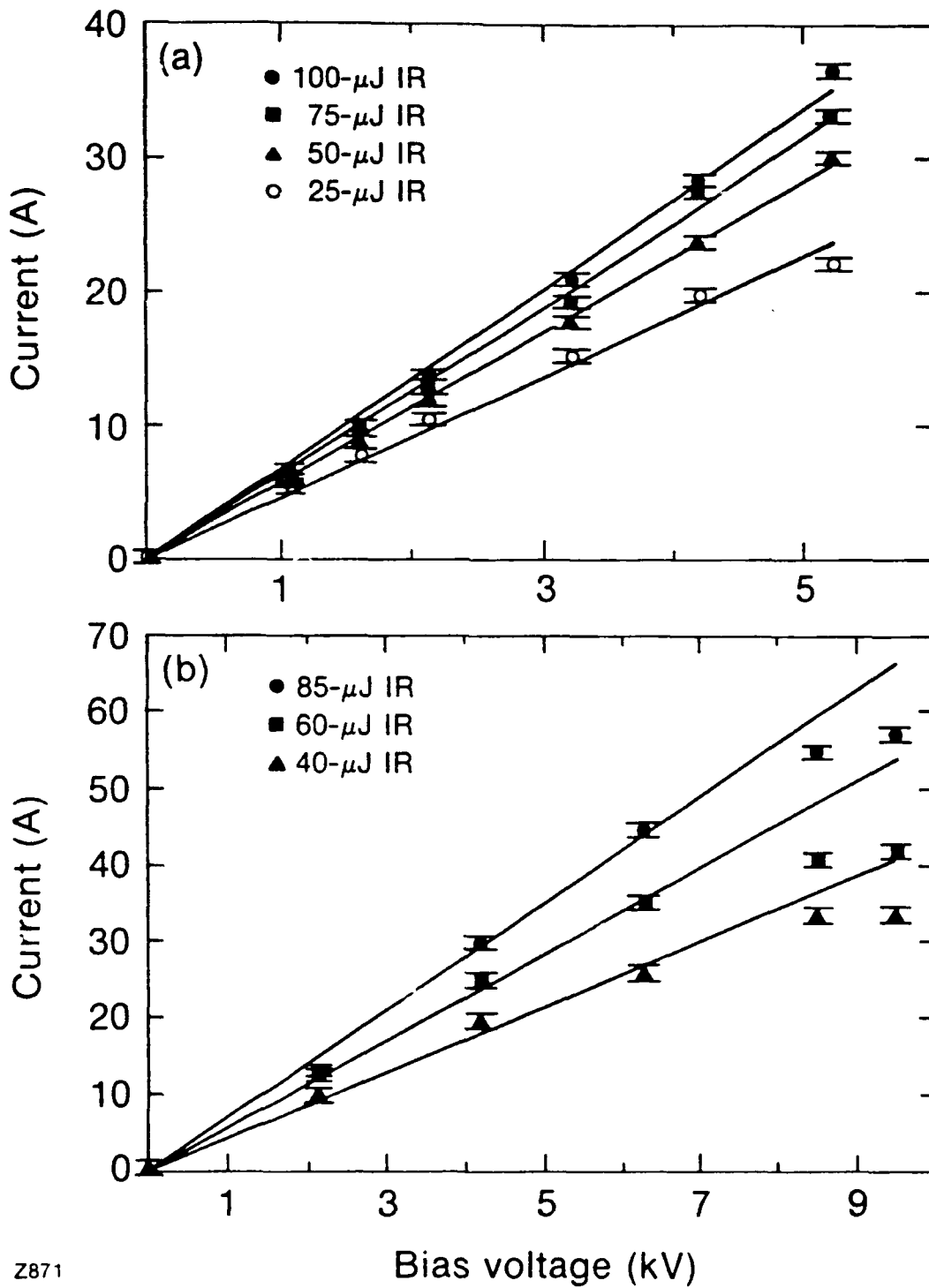
$$I_L = \frac{V_L}{Z} = \frac{1}{2Z + \frac{\ell}{Ane\mu}} V_{BIAS} \quad (8)$$

I_L should be a linear function of V_{BIAS} for a given optical pump energy, as the carrier density is proportional to the optical pump energy. Figure 15 illustrates results from measurements of I_L versus V_{BIAS} for various optical energies. The linear relationship between I_L and V_{BIAS} is verified for bias voltage up to 5 kV, as shown in Fig. 15(a). Figure 15(b) gives I-V curves for bias voltages up to 9 kV. The I-V curves deviate from linear behavior at high bias (>6 kV): the switch on-state resistance increases as the bias increases. This deviation from linearity coincides with the onset of negative differential resistance (NDR) in GaAs. Above ~ 3.2 kV/cm, the electron drift velocity in GaAs decreases as the electric field increases. Since the current is proportional to the drift velocity, this represents an effective increase in switch on-state resistance as the field increases above ~ 3 kV/cm and, therefore, we should not expect and do not see a continuation of the linearity between voltage and current. Thus, we have evidence to suggest the observed decrease in switching efficiency with increasing voltage is due to NDR, although the I-V measurements lack the temporal resolution of the imaging data. This observation has important implications for the use of photoconductive switches in pulsed power applications. In many cases, the trend has been to push the breakdown limit in these devices to achieve the highest switch electrical energy for the minimum optical energy. Our results indicate that switches with longer gaps, and lower field may be more efficient in terms of switched voltage to pump energy, at least in the purely photoconductive mode of switching for pulse durations of the order of 1 ns.

(B) Planar Switch Study

1. Motivation

GaAs surface switches were also investigated using the surface field probe geometry of Fig. 1; the principal focus of this work was the investigation of lock-on behavior in GaAs [19]. In GaAs the photo-generated electron hole pairs should recombine in about 1 ns. This should limit the duration of electrical pulses delivered with GaAs



Z871

Fig. 15 The load current versus bias voltage for various IR pump energies; (a) bias up to 5 kV; (b) bias up to 9 kV.

switches. Lock-on is the phenomenon where GaAs switches remain in the conducting state for a long time (hundreds of nanoseconds) after the optical excitation. This phenomenon was first reported by G. Loubriel *et al.* in 1987 [20,21]. It was observed that GaAs has two modes of operation. There is a low-field, or linear mode, where the voltage across the switch drops to zero as the laser pulse is applied, and after the laser pulse, the voltage recovers as the photogenerated carriers recombine at their characteristic rate. There is also a high-field, or nonlinear mode, where the switch voltage drops to zero during the laser pulse duration and tries to recover but does not regain its initial value. Instead, it locks on to some intermediate value, called the "lock-on" voltage, which is independent of the bias voltage for a given sample. This is a field dependent effect. The bias field has to be greater than a threshold value of 3 to 8 kV/cm for lock-on to occur. This threshold depends on the material preparation. In the lock-on state the voltage dropped across the sample is linearly proportional to the distance across which the voltage is dropped, the electrode spacing. Lock-on behavior has several interesting features, as reported by Zutavern: it can be triggered with very low light levels, $\sim 1/500$ the amount required to switch the same samples in the linear mode, therefore requiring some carrier gain mechanism; it requires light triggering, as biasing GaAs up to 140 kV/cm does not result in significant conduction; it persists for as long as the external circuit can provide current, maintaining the lock-on field across the switch [22].

The mechanism for lock-on is not understood. The threshold bias field for lock-on, 3–8 kV/cm, roughly corresponds to the threshold field for negative differential resistivity (NDR) in GaAs, and this suggests some connection between the two effects. Also, lock-on has been reported in Fe:InP, another semiconductor exhibiting NDR, and lock-on is not observed in Si or Au:Si, materials which do not exhibit NDR [23]. The Gunn effect alone can not be responsible for lock-on as it does not create carriers. An unknown carrier-generating process somehow connected to the Gunn effect may be responsible for lock-on. It is known that NDR can result in the formation of high-field regions (or Gunn domains)

in GaAs which repeatedly traverse the sample from the cathode to the anode [24]. For a given sample length, ℓ , the carrier density, n , in the sample must reach a critical value before domain formation occurs. The product of the sample length and carrier density, $n\ell$, obeys the relationship [25]

$$n\ell > 10^{12} \text{ cm}^{-2} \quad (9)$$

Propagating domains have been observed in samples of GaAs that were heavily doped to reach the critical carrier concentration, and domain formation is the basis for the well known Gunn diode [26]. Carriers can be generated in these high-field regions through impact ionization whereby electrons are accelerated by the high fields to sufficient energy (~ 2 eV) to create more electron-hole pairs and seed an avalanche, if the domain field is high enough (100–200 kV/cm). This effect can be explained by a phenomenological argument if we assume that at sufficient average field, a low light level trigger pulse supplies the critical carrier concentration for high-field domain formation. Avalanching produces the carriers which explain the trigger gain. If too many carriers are created, the resistance of the switch drops too low for the circuit to supply the lock-on field across the switch. Then the domains disappear and normal carrier recombination occurs [22].

This model does explain qualitatively some of the observed features of lock-on, including light trigger dependence, field dependence, and onset of lock-on during recovery of switch. It is dependent on the formation of Gunn domains in a GaAs photoconductive switch, an effect which had not previously been experimentally observed or predicted by a detailed theory. There is also some circumstantial evidence for the repeated formation of Gunn domains in GaAs switches in reports of current oscillations during switch operation [27], a behavior similar to a Gunn diode. We used the e-o imaging system to investigate the dynamic behavior of the electric field of a GaAs switch in the lock-on regime, one goal being to establish the existence of high-field regions during switch operation.

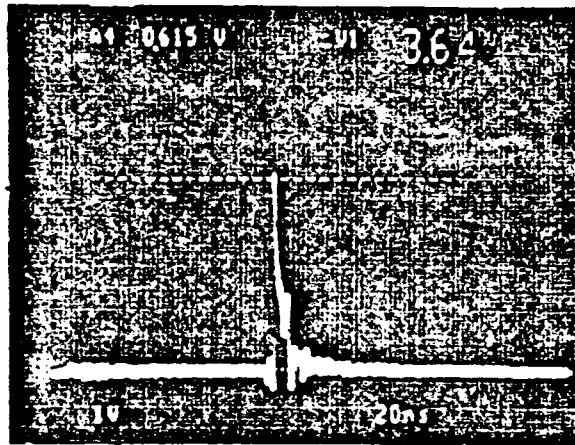
2. Planar Switch Data and Discussion

The GaAs switches used in the lock-on study were supplied by Sandia National Laboratory. They had two rectangular Ni:AuGe contact pads, 2.5 mm wide, and had an electrode spacing of 2.5 mm. The switches had an electron mobility of $7000 \text{ cm}^2/\text{volt-sec}$, an impurity concentration of 10^7 cm^{-3} , and an expected lock-on threshold of 4 kV/cm. To eliminate any complicating effects due to impurity concentrations, the photoconductive switching was done with 532-nm laser pulses (FWHM $\sim 140 \text{ ps}$), which have an energy greater than band gap allowing for direct band-to-band photoexcitation. The e-o probe pulses were infrared. The switches were installed in the switch holder used for the Si imaging. All switching experiments were performed with the switch under a pressure of $\sim 50 \text{ psi SF}_6$.

The lock-on behavior of the switch is seen clearly in Fig. 16, which shows oscilloscope traces of the switched output for bias voltage close to the lock-on threshold, 2.0 kV, and above the lock-on threshold, 3 kV. At 2.0 kV bias, the switch exhibits linear behavior, switching voltage only for a time consistent with normal recombination. At 3 kV bias, lock-on behavior is observed, with the switched output decaying normally until, at the onset of lock-on, the output voltage "restarts" for a second period of conduction lasting as long as the charging circuit supplies charge. Note that the lock-on effects occur several nanoseconds after the optical trigger pulse. To image the field during this period, the measurements were taken out to 6 ns after the trigger. A 6 ft optical rail was used in the pump delay line and the retroreflector was moved manually to obtain imaging data at this long delay. It was extremely difficult to maintain consistent illumination of the sample for delays longer than 6 ns due to the extremely long optical path change.

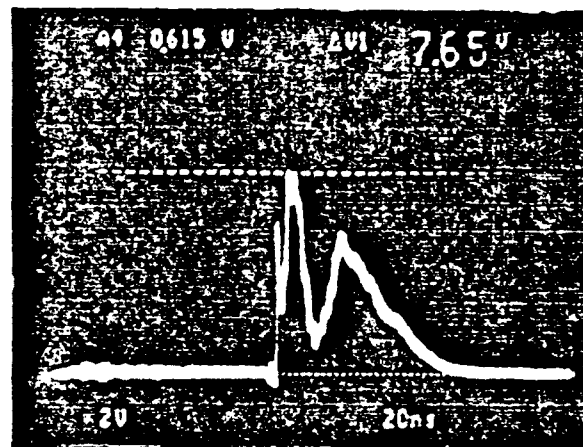
The e-o imaging measurements reveal a very complicated behavior. If one looks at the electric field averaged over the whole active area of the switch, two distinct patterns emerge. Below the threshold for lock-on, the field collapses uniformly in roughly the full width half maximum (FWHM) of the laser pulse. The rapid collapse is followed by a rapid

Below lock-on threshold



GaAs switch with 2.5-mm electrode gap;
2-kV bias; 8 kV/cm

Above lock-on threshold



GaAs switch as above with 3-kV bias;
12 kV/cm

Z838

Fig. 16 Oscilloscope traces of switched output waveform of planar GaAs switch monitored at the load using current probe for (a) -2.0 kV bias, just at lock-on threshold; and (b) -3.0 kV, above lock-on threshold. The time scale is 20 ns/div.

recovery of the order of a few hundred picoseconds followed by a slower recovery to the initial bias field in about 5 ns. This trend is illustrated in Fig. 17, which shows the average electric field along a line parallel to the contacts and through the center of the contacts for a switch bias of 2.5 kV (10 kV/cm).

Above the threshold for lock-on the behavior is more complicated. The field collapses and starts to recover as in the below-threshold case. However, at about 1 ns after the pump pulse, the field begins to collapse again. The second collapse of the electric field across the switch is much slower than the first, optically induced, collapse. It is also not monotonic. An oscillatory structure is superimposed on the decay of the electric field. Figure 18, which is similar to Fig. 17, illustrates the gross features described above, switch bias 6 kV (24 kV/cm). This second decrease in the electric field is apparently associated with the lock-on state. Oscilloscope traces for a current probe at the output of the switch biased at 6 kV were similar to Fig. 16(b), indicating that conduction through the switch continued longer than would be expected from that determined by the recombination of the electron-hole pairs.

The temporal evolution of the spatial profile of the electric field above the switch is shown for bias voltages of 2.5 kV and 6 kV in Figs. 19 and 20, respectively. In both figures, the field collapses in about the 140 ps FWHM of the pump pulse, collapsing most rapidly in the center of the gap. This rapid collapse in the switch center is much more than would be expected from the ~10% contact-to-contact spatial variation in pump energy due to the Gaussian profile of the pump. As the field recovers due to carrier recombination, the field at the negative high-voltage contact (the cathode) rises rapidly, forming a local region of high field. This is most pronounced at 6 kV bias (above lock-on), where the high-field domain can be seen to be extending from the cathode, propagating across the switch.

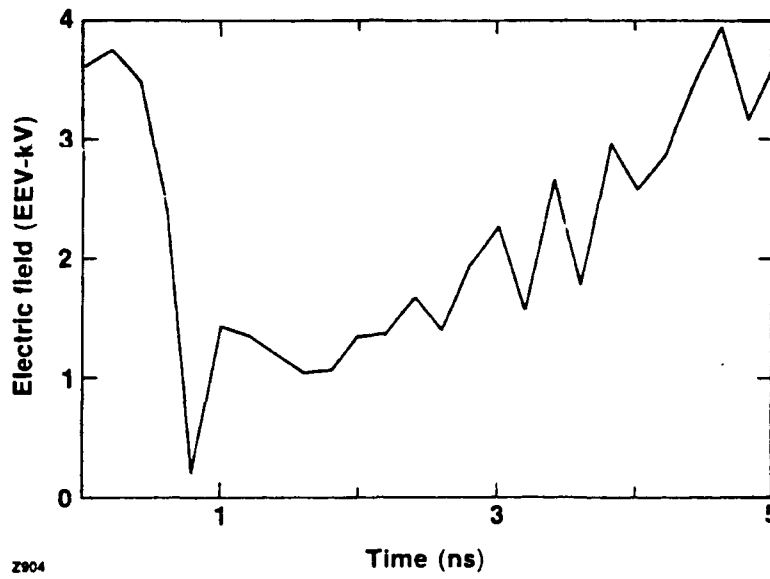


Fig. 17 Average electric field above active area of planar switch as a function of time at -2.5 kV bias voltage, just below lock-on threshold for this sample. Each data point in this plot is an average over all pixels in the active region of the electro-optic field image.

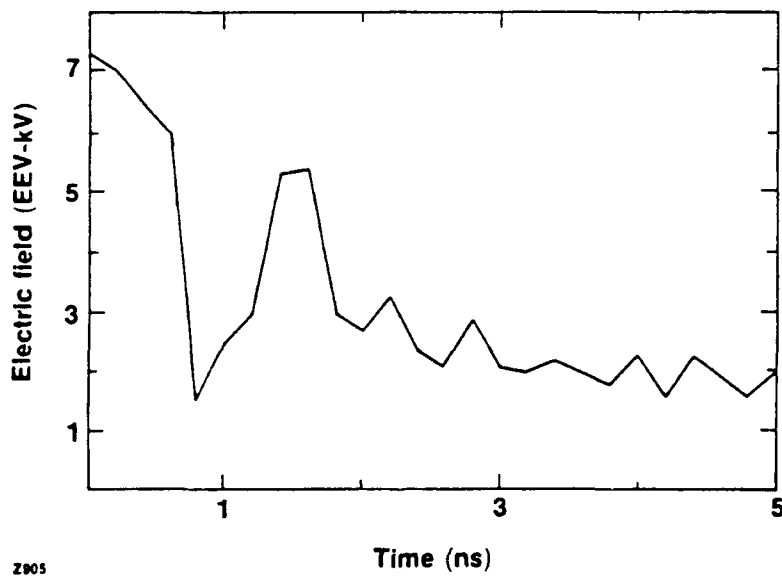
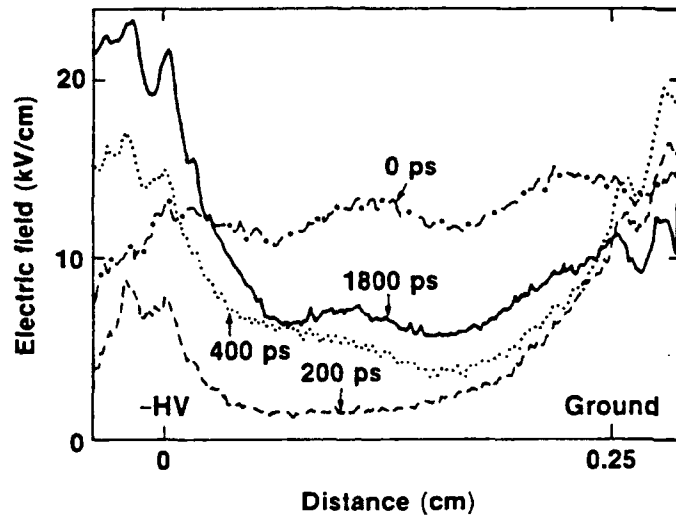
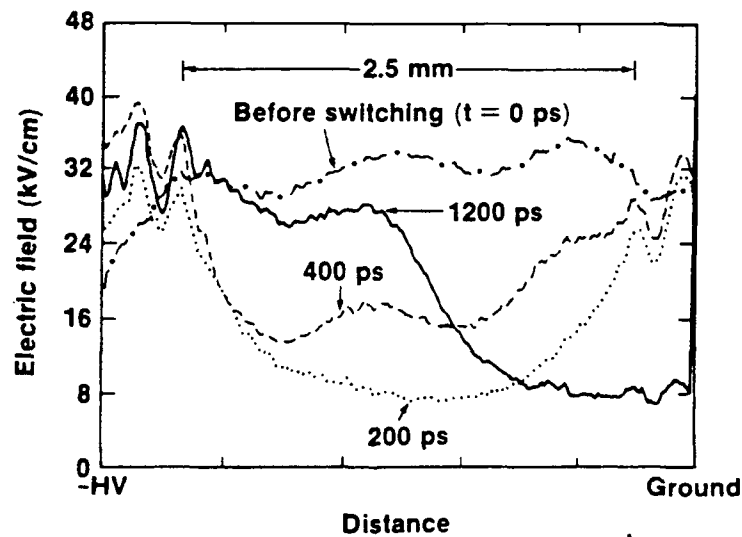


Fig. 18 Average field versus time, as in Fig. 17, at bias of -6 kV, above lock-on threshold.



Z899

Fig. 19 Electric field spatial profiles above planar switch along a line between the switch contacts at different times during switch operation. This plot was obtained from the full electro-optic image by averaging over 100 pixels along a direction parallel to the contact edge. The switch bias was -2.5 kV (10 kV/cm). 0 ps is just before pump pulse arrival. Note field enhancement at contact edges at 0.0 cm and 0.25 cm.

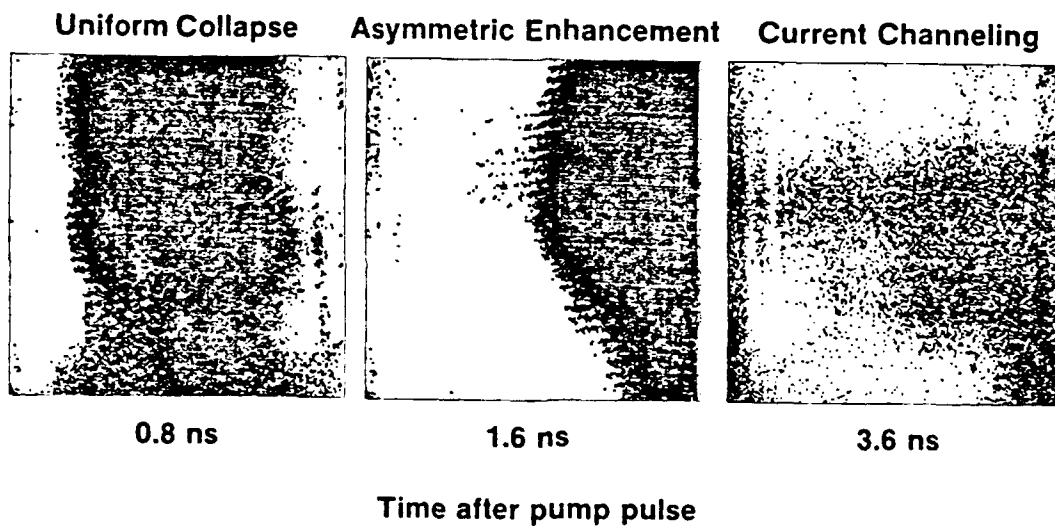


Z898

Fig. 20 Electric field profiles at different times, as in Fig. 19, switch bias -6 kV (24 kV/cm). Note high-field domain extending from cathode.

These graphs reveals only a small portion of the complex behavior of these devices. Figure 21 shows three different electro-optic images at different times after illumination. The images have been manipulated so that a dark region in the active switch area indicates the absence of an electric field greater than 16 kV/cm. A white region indicates the presence of an electric field greater than 16 kV/cm. Figure 21(a) shows the electric field at the peak of the photo-induced conductivity. The active area of the switch is uniformly black, indicating complete switching, and the edges of the contacts are clearly delineated. At time beginning about 1 ns after complete switching has occurred the electric field develops a 2-D structure. In some places the field has collapsed and in other places it has increased to values which may even be greater than the original applied field. In Fig. 21(b), which occurs 0.8 ns after Fig. 21(a), the electric field is concentrated near the high voltage contact. This image is 400 ps in time after the lineout in Fig. 20 at 1200 ps showing the propagating domain. This then evolves into the state shown in the last image, Fig. 21(c). A region of low field, which indicates the presence of carriers in the underlying semiconductor, extends out from the low voltage contact. This corresponds to a local region of high conductivity extending across the switch. Note that this region is only about 25% of the active area of the switch and may indicate that the current is being carried in channels through the switch in the lock-on regime.

The images in Fig. 21 are representative of the many images taken of the GaAs switch operation. A survey of all the images show that the field is changing everywhere in the switch gap, with a proponderance of the images showing field domains at the cathode and indications of current channeling. As previously discussed, high-field domain formation is associated with NDR in GaAs. Current channeling, also, is a manifestation of NDR [26]. From the imaging data, we observe that above the lock-on threshold bias voltage (the 6 kV data), high-field domains develop at the switch cathode during the switch recovery and there are indications that the switch current is being carried in channels. We



Black < 16 kV/cm; white > 16 kV/cm

Z870

Fig. 21 Electro-optic images at different times during planar switch operation. The images have been processed so that white corresponds to field >16 kV/cm and black is <16kV/cm. Time is relative to pump pulse arrival. The image progresses from complete switching in (a), to formation of high-field domain (b), to channels of low field (c).

conclude that these effects are caused by the NDR in GaAs, which is verified by the computer-assisted analysis.

IV. COMPUTER-AIDED ANALYSIS OF PHOTOCONDUCTIVE SWITCHING

We present a model of photoconductive switch behavior that is based on the time-dependent, drift-diffusion equations and carrier continuity equations. The equations were appropriately modified to represent a photoconductor in operation and then solved numerically with boundary conditions and operating parameters that are consistent with high-speed switching of a practical, high-voltage, photoconductive switch in an external circuit. High-field, nonlinear effects, such as negative differential resistivity in GaAs and impact ionization, are included in the model. The results of the experiments are discussed in terms of this computer model.

(A) Model Formulation

On the time scale of ultrafast, high-power photoconductive switch operation, picoseconds to nanoseconds, transient photoconductivity is governed by the generation, recombination, and transport of carriers. Hot electron effects, drift velocity overshoot, and other nonequilibrium processes such as inter-valley transfer of electrons are significant on a subpicosecond, or femtosecond time scale, and need not be included in a model of high-voltage switch operation on a multipicosecond time scale. On this timescale, the carrier mobility, μ , for example, is assumed to have reached its steady-state value so that DC measurements that depend on the drift velocity versus field relationship, e.g. an I-V curve, are valid. The spatial and temporal variations of the carrier densities, electric field, and potential in the switch on a picosecond time scale are given by the solutions to the coupled system of equations commonly referred to as the drift-diffusion equations, without requiring Monte Carlo type calculations for the electron energy distribution. A study of femtosecond

transient photoconductivity utilizing Monte Carlo calculations has been presented by Meyer [28].

Using the drift-diffusion/carrier continuity model, Iverson has previously modeled photoconductors operating in a nonswitching, or small-signal, mode where the potential across the switch does not vary appreciably [29,30], and the switching, or large-signal mode, where the bias voltage across the photoconductor is quickly switched to an external load [31]. This photoconductive switching model dealt with large-scale, practical high-power switches, but did not include nonlinear carrier mobility. Weiner *et al.* have also presented a solution to the semiconductor equations in high-bias switches for the constant mobility, or linear, regime [32]. This model did not include carrier diffusion. White *et al.* [33] have constructed a computer model of high-bias photoconductive switching, numerically solving the drift-diffusion/carrier continuity relations, that includes nonlinear mobility, but this model deals only with micron-scale device lengths and relatively low bias voltages (<1 kV) and is not capable of simulating a more realistic, cm-scale device with multi-kilovolt bias voltage. Sano and Shibata have presented a very complete, three-dimensional model of ultrafast switches in microstrip lines [34], but this model is limited by computer memory requirements to 100- μm size devices and total simulation times of only a few picosecond; results were only presented for a 2.5 V bias voltage. The model presented here is the first numerical solution of the semiconductor device equations capable of simulating ultrafast photoconductive switches under operating conditions consistent with realistic pulsed-power applications that includes nonlinear carrier mobility.

1. Model equations

We have modeled photoconductive switches as one-dimensional devices in terms of current flow and assumed effects perpendicular to the applied bias field are of second order and may be neglected. The problem can then be posed in one spatial variable and in one spatial direction along the applied bias field. Call this variable x , $x \in (0, \ell)$, where ℓ is the

switch electrode gap. Also, as the photogenerated, or excess densities, are typically many orders of magnitude greater than the thermal equilibrium densities, the carrier densities in the previous equations can be considered to be the excess densities, with the small thermal equilibrium values of the electron and hole densities neglected. Figure 22 shows the photoconductive switch and circuit, illumination schemes, and variables used in this model.

The one-dimensional forms of the semiconductor device equations are given below

$$\frac{\partial n(x,t)}{\partial t} = G(x,t) - R_n(x,t) + \frac{1}{e} \frac{\partial}{\partial x} J_n(x,t) \quad (10)$$

$$\frac{\partial p(x,t)}{\partial t} = G(x,t) - R_p(x,t) - \frac{1}{e} \frac{\partial}{\partial x} J_p(x,t) \quad (11)$$

$$J_n(x,t) = e\mu_n(x,t)n(x,t)E(x,t) + e D_n(x,t) \frac{\partial}{\partial x} n(x,t) \quad (12)$$

$$J_p(x,t) = e\mu_p(x,t)p(x,t)E(x,t) - e D_p(x,t) \frac{\partial}{\partial x} p(x,t), \quad (13)$$

$$\frac{\partial^2}{\partial x^2} \Psi(x,t) = -\frac{e}{\epsilon} [p(x,t) - n(x,t)] \quad (14)$$

$$E(x,t) = -\frac{\partial}{\partial x} \Psi(x,t) \quad (15)$$

$$D_n(x,t) = \mu_n(x,t) \frac{kT}{e} \quad (16)$$

$$D_p(x,t) = \mu_p(x,t) \frac{kT}{e} \quad (17)$$

Equations (10) – (17) are a system of nonlinearly coupled, parabolic/elliptic partial differential equations. This system is solved for the particular functions, $R(x,t)$ and $G(x,t)$, and initial values and boundary conditions appropriate for photoconductive switch operation.

Diffusion of carriers can be included in the model even though the applied bias voltage is vastly greater than the thermal voltage, $\frac{kT}{e}$, which is $\cong 0.03$ V at room temperature. It would appear that the drift component of the current would dwarf the diffusion term. However, as the electric field collapses to a very low value when the switch

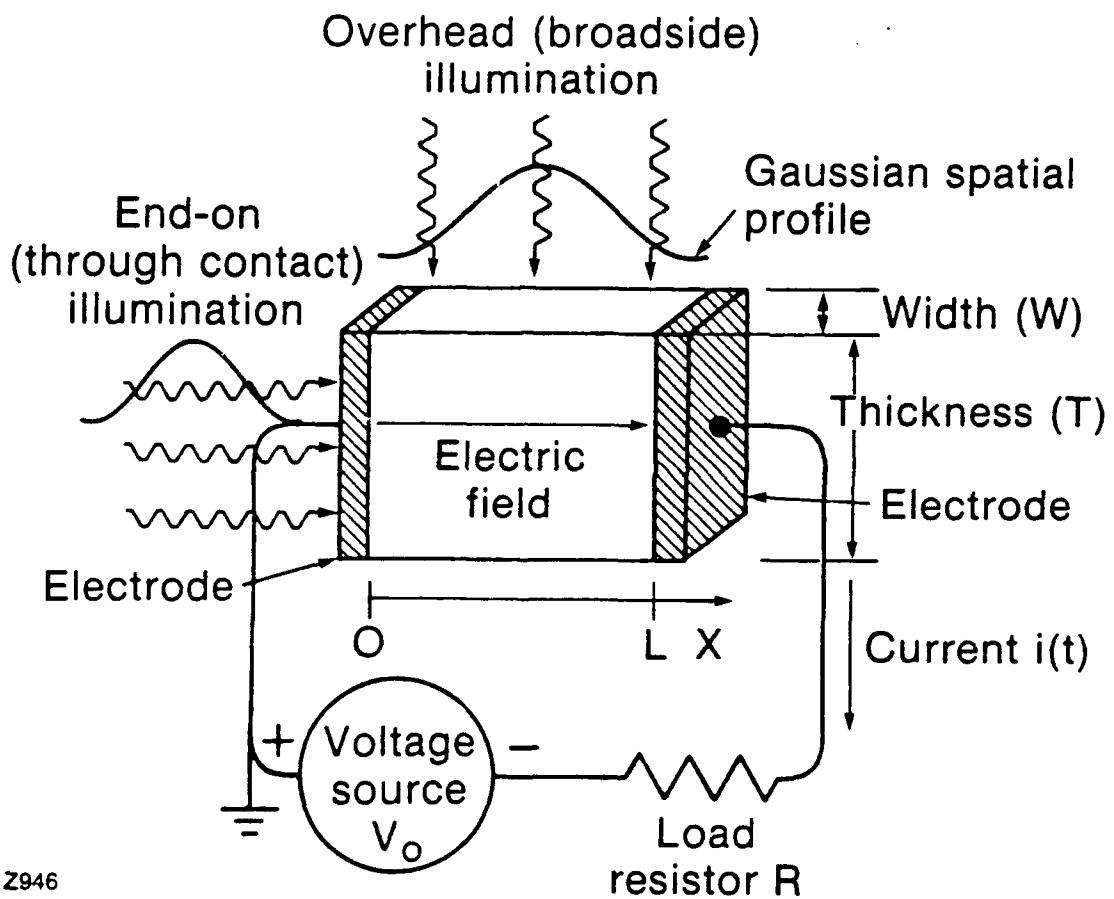


Fig. 22 Photoconductive switch and external circuit as modeled in computer simulation. Model variables, parameters, and illumination schemes shown.

closes, the diffusion current may become comparable to the drift current. Also, diffusion can be significant if very large carrier density gradients develop. The inclusion of diffusion also completes the model mathematically. We can choose to run simulations without diffusion, as well.

(a) Carrier generation functions

The function $G(x,t)$ represents the generation of carriers. $G(x,t)$ can be written as the sum of two parts

$$G(x,t) = G_{opt}(x,t) + G_{imp}(x,t) \quad (18)$$

$G_{opt}(x,t)$ is the electron-hole pair generation rate due to photoexcitation by laser light and $G_{imp}(x,t)$ is the generation rate due to the excitation of electron-hole pairs through impact ionization.

The form of $G_{opt}(x,t)$ depended on the particular illumination scheme that was simulated. In all cases, the number of carriers created was assumed proportional to the optical energy absorbed and the optical pulse was assumed to have a normalized Gaussian temporal profile. In general, $G_{opt}(x,t)$ can be written

$$G(x,t) = \phi(x) \frac{N_0}{a\sqrt{2\pi}} e^{-\frac{(t-t_0)^2}{2a^2}} \quad (19)$$

where N_0 is the total number of photons in the optical pulse, a is the temporal variance of the optical pulse ($a = \frac{FWHM}{2\sqrt{\ln(4)}}$), and $\phi(x)$ will depend on the particular spatial illumination scheme. Overhead, or broadside, illumination, and end-on, through the contact, illumination were simulated. For end-on illumination, t in Eq. (18) is replaced by $t \rightarrow t - x/c$ to represent a Gaussian pulse propagating through the switch from $x = 0$, or $t \rightarrow t - (\ell - x)/c$ for a light pulse propagating from $x = \ell$. The amount t_0 is subtracted from t to shift the peak optical intensity away from $t = 0$ so that illumination begins t_0 before the peak

of the optical pulse (typically at ~1% of the peak intensity). For uniform overhead illumination, $\phi(x)$ is given by

$$\phi(x) = \frac{1}{\ell wd} \quad (20)$$

where $A = wd$ is the area of the conducting region of the switch, and ℓA is equal to the conducting volume. For a normalized Gaussian spatial laser beam profile,

$$\phi(x) = \frac{1}{b\sqrt{2\pi}} \frac{1}{A} e^{-\frac{(x-ctr)^2}{2b^2}} \quad (21)$$

where b is the spatial variance of the optical beam, and ctr is the center of the illumination. Asymmetric illumination can be simulated by giving ctr a value other than $\ell/2$. For end-on illumination through $x=0$, $\phi(x)$ is written

$$\phi(x) = \frac{\sigma}{wd} e^{-\sigma x} \quad (22)$$

where σ is the absorption coefficient of the semiconductor for the optical pulse. For illumination through $x = \ell$, x in Eq. (23) is replaced by $x \rightarrow \ell - x$.

Intrinsic impact ionization occurs when a carrier gains enough energy through acceleration in an electric field to directly generate an electron-hole pair through collision. The electron-hole generation rate due to impact ionization is given by

$$G_{imp}(x,t) = \alpha_n n(x,t) v_{dn}(x,t) + \alpha_p p(x,t) v_{dp}(x,t) \quad (23)$$

where α is defined as the number of electron-hole pairs generated by a carrier per unit distance traveled. α_n and α_p are strongly dependent on the electric field. The forms of α used in this model were obtained by fitting expressions given by Sze to experimental data also presented in Sze [35]. The model expressions for α are given in Table 1.

Table 1	
Model Impact Ionization Parameters	
<i>GaAs</i>	
Electrons	$\alpha_n(E) = 0.173 \text{ V}^{-1} E e^{\frac{-3.64 \times 10^{11} \text{ V}^2/\text{cm}^2}{E^2}}$
Holes	$\alpha_p = \alpha_n$
<i>Silicon</i>	
Electrons	$\alpha_n(E) = 1.1016 \text{ V}^{-1} E e^{\frac{-9.242 \times 10^5 \text{ V}/\text{cm}}{E}}$
Holes	$\alpha_p(E) = 3.420 \text{ V}^{-1} E e^{\frac{-1.766 \times 10^6 \text{ V}/\text{cm}}{E}}$
E is the electric field in V/cm (after Ref. [35])	

(b) Reduction function

The function $R(x,t)$ represents the reduction of carriers through recombination processes. Only direct recombination of electrons with holes is considered, leading to the simple expressions for the hole and electron recombination rates

$$R_n(x,t) = R_p(x,t) = \frac{\text{minimum of } \{ p(x,t) ; n(x,t) \}}{\tau} \quad (24)$$

where τ is the carrier recombination time. The minority carrier density determines the recombination rate as more electrons, for example, cannot recombine than there are holes with which to recombine. It was chosen to write $R(x,t)$ as Eq. (24) as this form is symmetric and does not create charge. It is possible to use more complex forms for $R(x,t)$, such as trap-assisted Shockley-Read-Hall recombination, which would provide more fitting parameters, but Eq. (24) proved adequate for our simulations.

(c) Carrier Mobility

The electric field dependence of the carrier mobility is included in the model. It is necessary to include this nonlinear effect to properly simulate photoconductive switching at

high-bias fields. The field-mobility relation for GaAs used by Horio *et al.* [36] was used. For Si, the relationship given by Sze was used [37].

(B) Numerical Solution Method

The practical units of high-power switching are picoseconds, centimeters, and volts. It was chosen to dimensionalize all equations in these units. All independent variables and constants were normalized to picoseconds, centimeters, and volts.

The redimensionalized model equations were then solved numerically. The equations were first put into a discrete form using a finite difference representation. Centered difference representations [38] are used for the density gradients in Eqs. (12)–(13), second derivative of the potential in Eq. (14), and potential gradient in Eq. (15). The divergence of the current density in the continuity equations is represented using an upwind-differencing scheme [39]. The spatial discretization is carried out on a uniform mesh, dividing the domain $(0, \ell)$ into equally spaced mesh points. Both 500-point and 250-point meshes were used. A fully explicit, forward time finite difference scheme is used for the time derivatives in the continuity equations.

A computer program, written in FORTRAN, was used to solve the system of finite difference equations. First, at the start of each time step, the carrier generation function for that time step is calculated. Then, using the density values calculated in the last time step or from the initial conditions, the electric potential at each mesh point is determined. This is done by using the Thomas algorithm [40] to solve the tri-diagonal system of simultaneous algebraic equations resulting from the discretization of Poisson's equation. The electric field is then determined from the potential, and the carrier mobilities from the field-mobility relations. Next, the current densities are evaluated at each mesh point. The carrier continuity equations are integrated forward in time determining the new carrier densities, which will be used in the next time step. The differential equation for the potential at the right-hand endpoint is also integrated forward in time, yielding a new value to be used in

calculations in the next time step. The integral required by the boundary condition equation was evaluated using a Simpson's rule quadrature scheme. All variables are renewed and the process is iterated until the desired device operation time has been simulated.

The fully explicit time integration scheme, while requiring relatively little storage, places a severe restriction on the discrete timestep that may be used. Stability was achieved using time and space steps, Δt and Δx , that satisfy the Courant stability criterion, $\Delta x < v\Delta t$, where v is the speed of the fastest phenomenon in the modelled system [41]. v was taken to be the speed of light in the semiconductor. Timesteps four times smaller than those demanded by the Courant condition were typically used to obtain accurate results. Program accuracy was determined by comparing numerical results for simple test cases with the analytical solutions.

(C) Computational Results

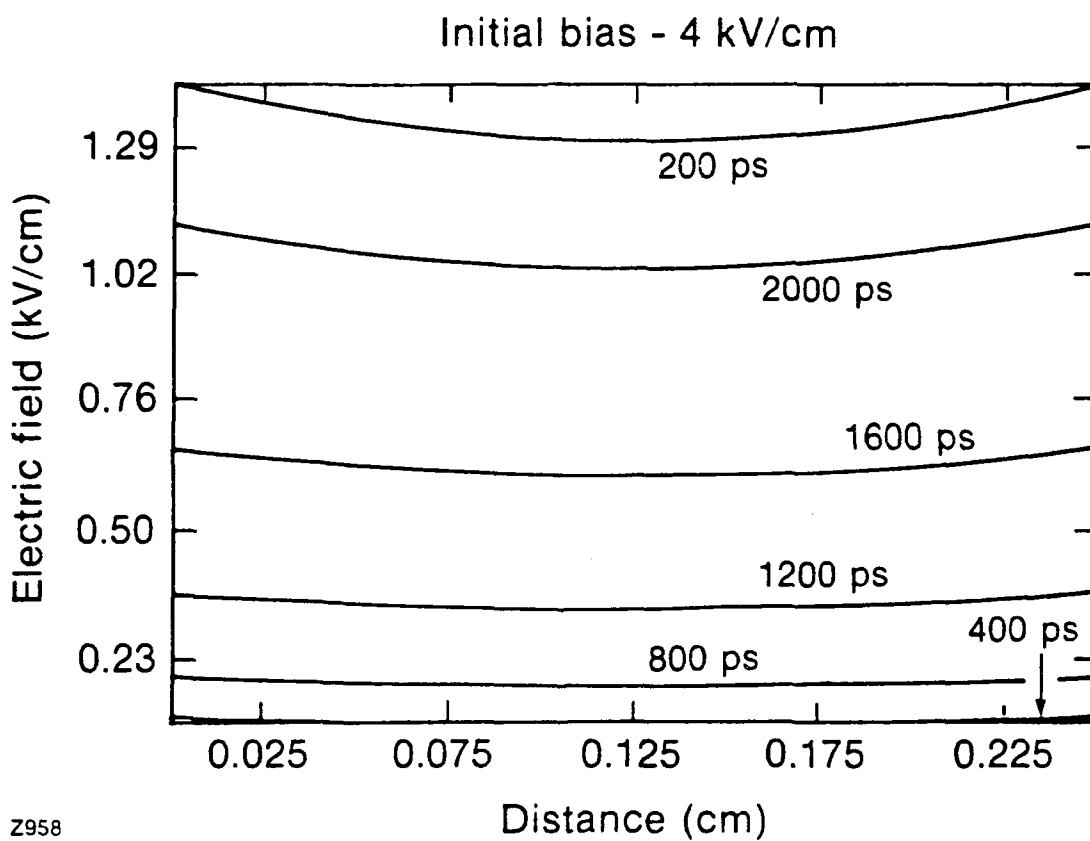
Simulations were run for operating parameters consistent with the experiments that were carried out. The illumination schemes, optical pulse intensities, device dimensions, bias voltages, and boundary conditions were set to recreate the actual conditions as closely as possible. A Digital Equipment VAX and a CYBER 990 computer were used to run the simulations. In the course of the computations it was found that carrier diffusion did not play a significant role in photoconductive switch operation and could actually lead to instabilities in the numerical results. This is due to an instability inherent in equations containing both convection and diffusion terms. There is a special numerical technique for dealing with this instability, namely the upwind differencing scheme of Scharfetter and Gummel [42], although this finite-difference formulation obscures the physics of the problem. We eliminated carrier diffusion from our model after establishing its relative unimportance.

1. Gallium arsenide switching

(a) Coplanar Switches

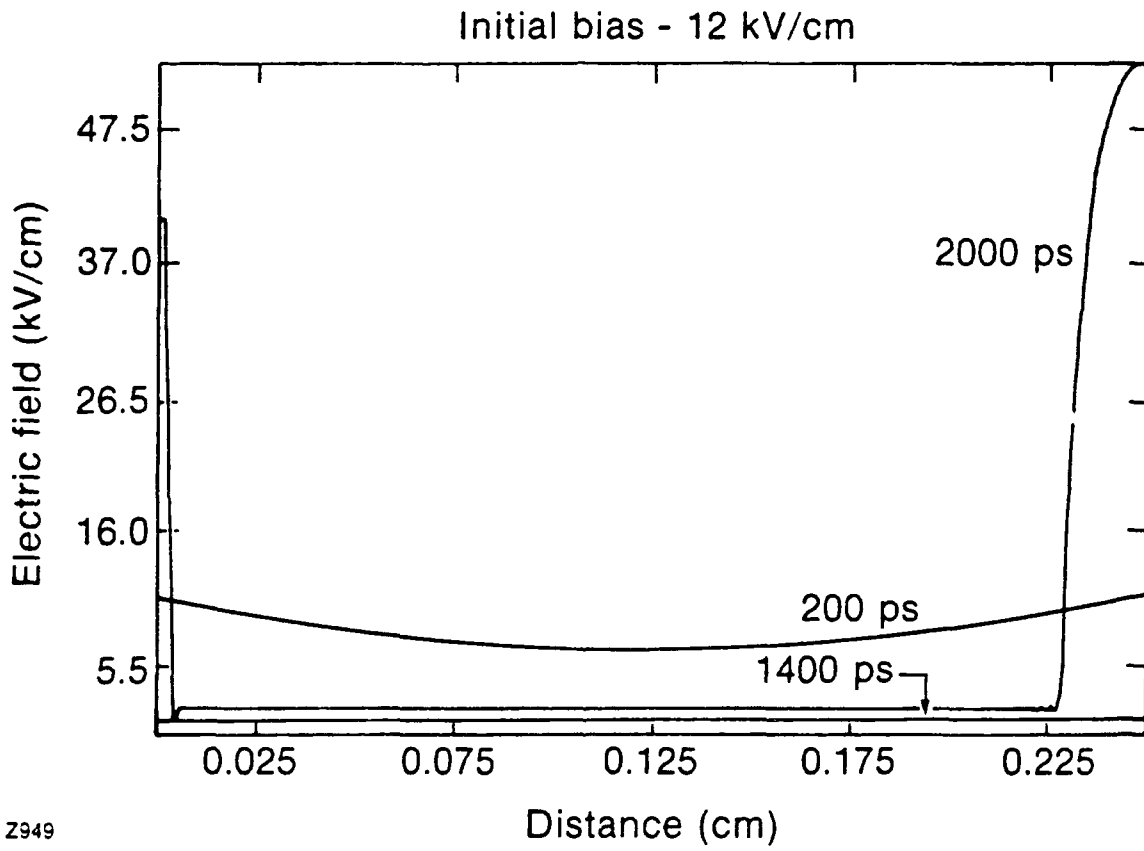
The operation of the coplanar GaAs switches was simulated. For these switches, $l = 0.25$ cm, $w = 0.25$ cm, and $d = 0.05$ cm. A value of $\epsilon = 13.1$ was used for the the permittivity of GaAs [43]. The simulation carrier lifetime was 600 ps. The optical pulse FWHM was 140 ps. Overhead illumination by Gaussian spatial profile optical beams was modeled, using model parameters matching experimental conditions. The spatial profile of the optical beam had ~10% energy imbalance between the ends of the switch and the switch center. The optical pulse energy was 50 μ J and the pump wavelength was 532 nm, resulting in carrier densities of $\sim 10^{16}/\text{cm}^3$. The negative high voltage is applied at $x = 0.25$ cm. The electric field is positive if it is in the positive direction of x : the bias field is positive.

Computed values of the electric field spatial profile are shown in Figs. 23, 24, and 25. Calculated profiles are shown for bias voltages of -1 kV, -3 kV, and -6 kV. The corresponding experimentally obtained profiles for -2.5 kV and -6 kV are shown in Figs. 17 and 18. The simulated and observed profiles are in excellent qualitative agreement. The -1 kV bias voltage field profile, corresponding to a bias field of 4 kV/cm, displays linear behavior: the initial bias field collapses in time effectively to zero and then recovers as the carrier density decreases due to recombination. The slight, symmetrical increase in field at the contacts is the result of the Gaussian spatial profile of the pump beam. As the bias voltage in the simulation is increased to -3 kV, the field becomes strongly enhanced at the contacts, with a field spike beginning to form at the cathode as the carrier density decreases due to recombination. This field enhancement is displayed in the e-o image lineout, as well. As the voltage is increased, this field enhancement at the cathode becomes the salient feature of the field profiles. At -6 kV bias, the simulated field at the cathode is higher than the initial bias field of 24 kV/cm. This high field domain can be seen to be moving toward the ground contact. The domain velocity is $\sim 1 \times 10^7$ cm/s.



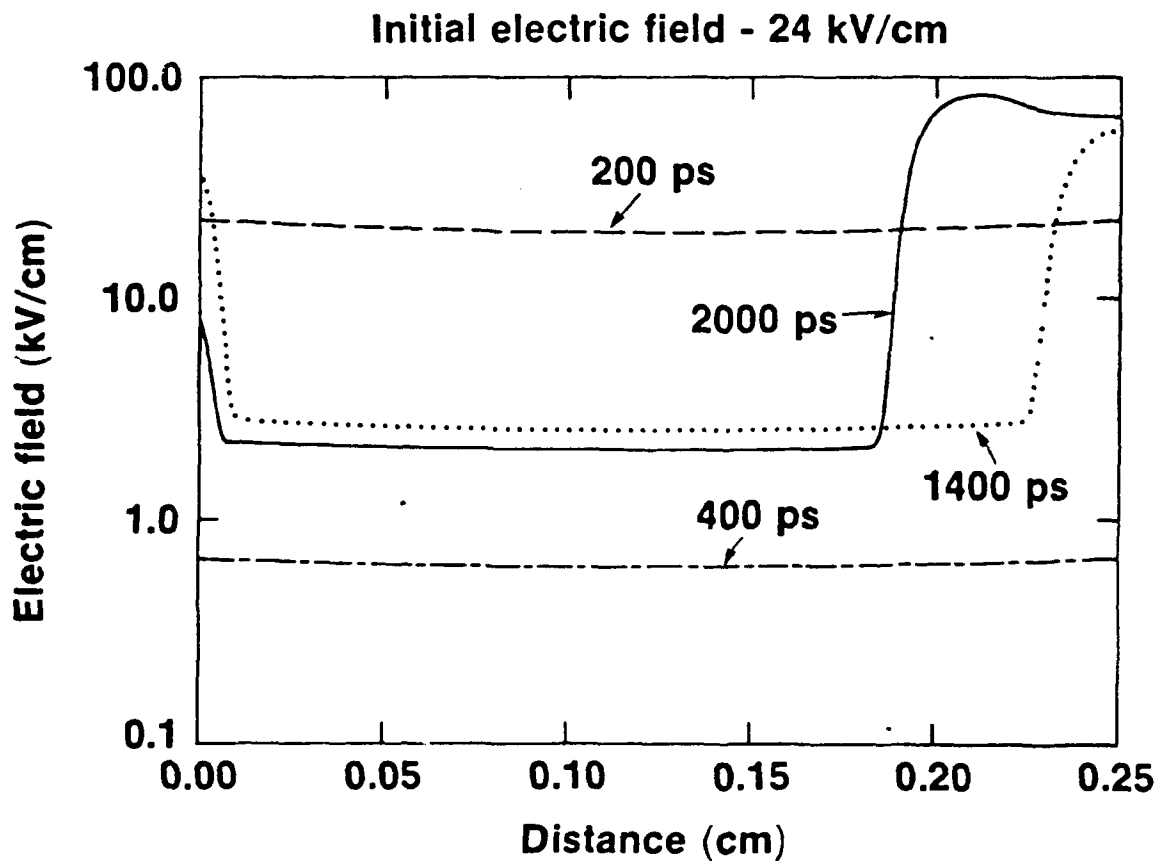
Z958

Fig. 23 Calculated spatial profile of electric field in GaAs switch biased at -1 kV at different times during switch operation. The electric field displays uniform collapse and recovery at this bias voltage.



Z949

Fig. 24 Electric field spatial profiles for GaAs switch -3 kV bias.



Z903

Fig. 25 GaAs switch electric field spatial profiles for -6 kV bias.

Simulations for longer times show a second domain will nucleate the cathode. The formation of a high-field domain at the cathode is also observed in the experimental profile, although the field enhancement is not the same magnitude as in the simulations. Figure 26 shows the simulated electric field profile for -6 kV bias on an expanded time scale, emphasizing the initial optically-induced collapse of the field. The simulated profile shows the same rapid collapse in the switch center, not directly related to the pump spatial profile, as is observed in the experimental lineouts in Figs. 24(b) and 25(b) for $t < 400$ ps.

The calculated switch output waveform for -6 kV bias is shown in Fig. 27. The average electron density in the switch is also shown. Lock-on effects, such as persistent output current, are not recreated in simulated GaAs output waveforms. On the basis of this model's results, intrinsic impact ionization is not responsible for lock-on. Some other carrier gain mechanism, whose effects are appreciable at lower fields, may be appropriate. Impact ionization of traps is a possibility.

The corresponding electron density profile for the simulated -6 kV bias profile in Fig. 25 is shown in Fig. 28. There is a propagating density disturbance which corresponds to the high-field domains in the electric field profile. Figures 25 and 28 are consistent with previous calculations [44] and experiments [45] for GaAs Gunn diodes.

To determine the cause of the high-field domains, numerous simulations were run, including various nonphysical situations, such as constant mobility, extremely long carrier lifetimes, etc. Only those simulations including nonlinear carrier mobility exhibited high-field formation. The formation of domains in the calculated data was influenced by the illumination profile parameters and the simulation recombination time, and occurred only during the recovery of the switch. Gunn domains are not observed in the modeling of switching in Si for any combination of parameters. The formation of high-field domains is a result of negative differential resistance in GaAs.

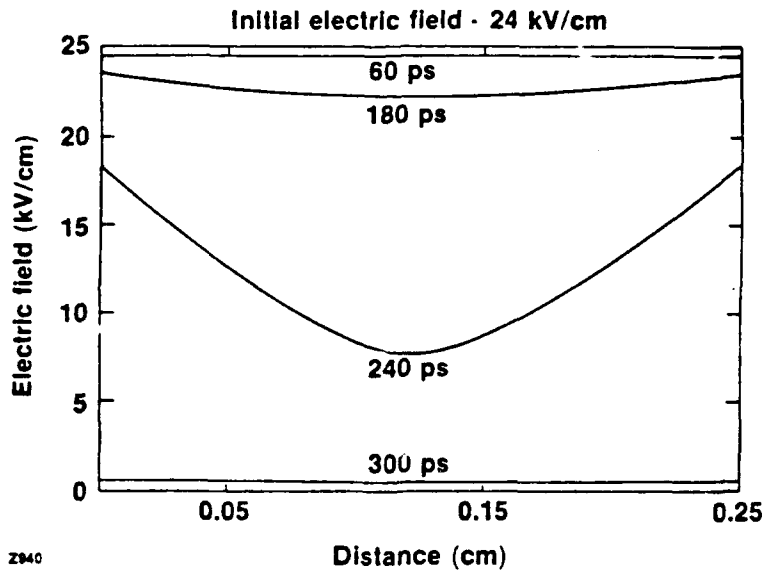


Fig. 26 Calculated electric field profile at -6 kV bias as in Fig. 25(a) with emphasis on early collapse of field. Note the field collapses most rapidly in the switch center.

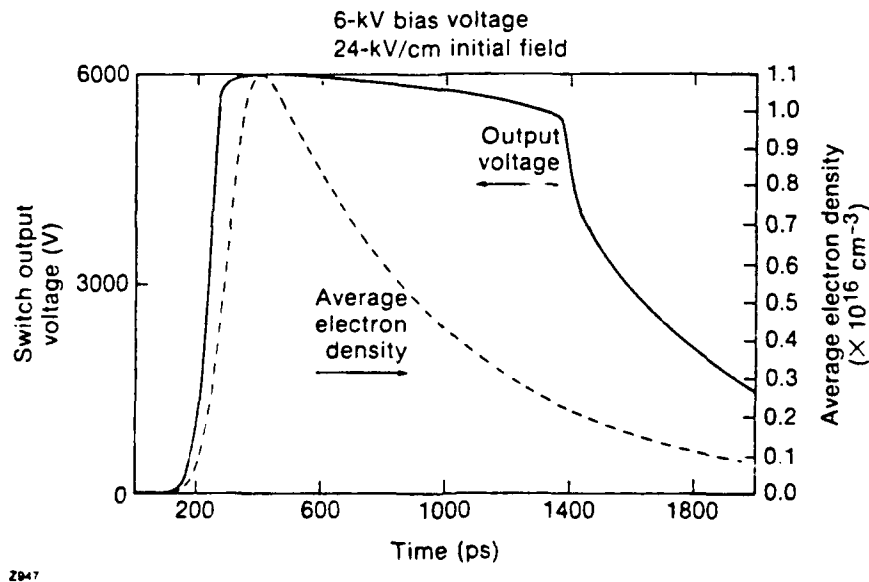
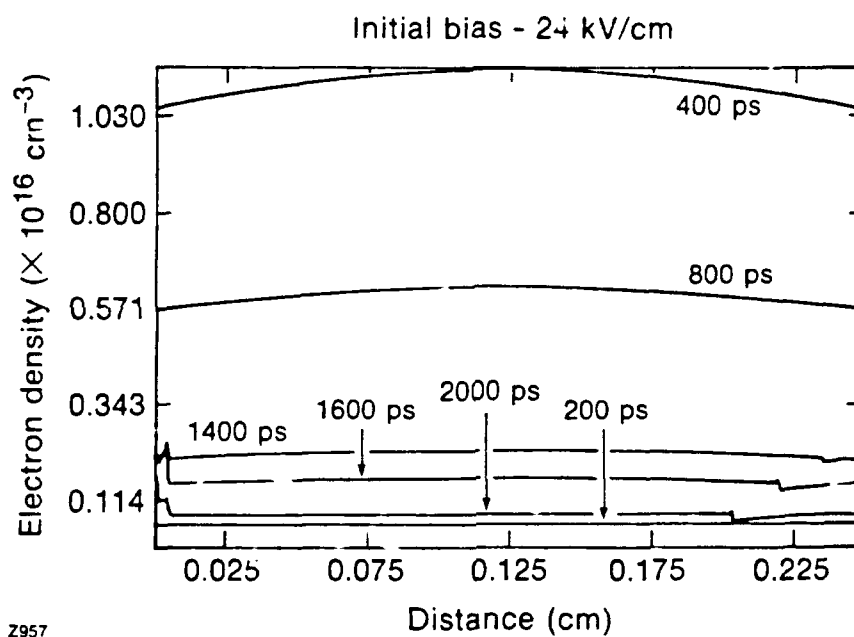


Fig. 27 Simulated GaAs switch output waveform at -6 kV bias. The average electron density in the switch is also shown.



Z957

Fig. 28 Calculated electron density spatial profile in GaAs switch at different times during switch operation. Note the propagating density disturbance for times ≥ 1400 ps.

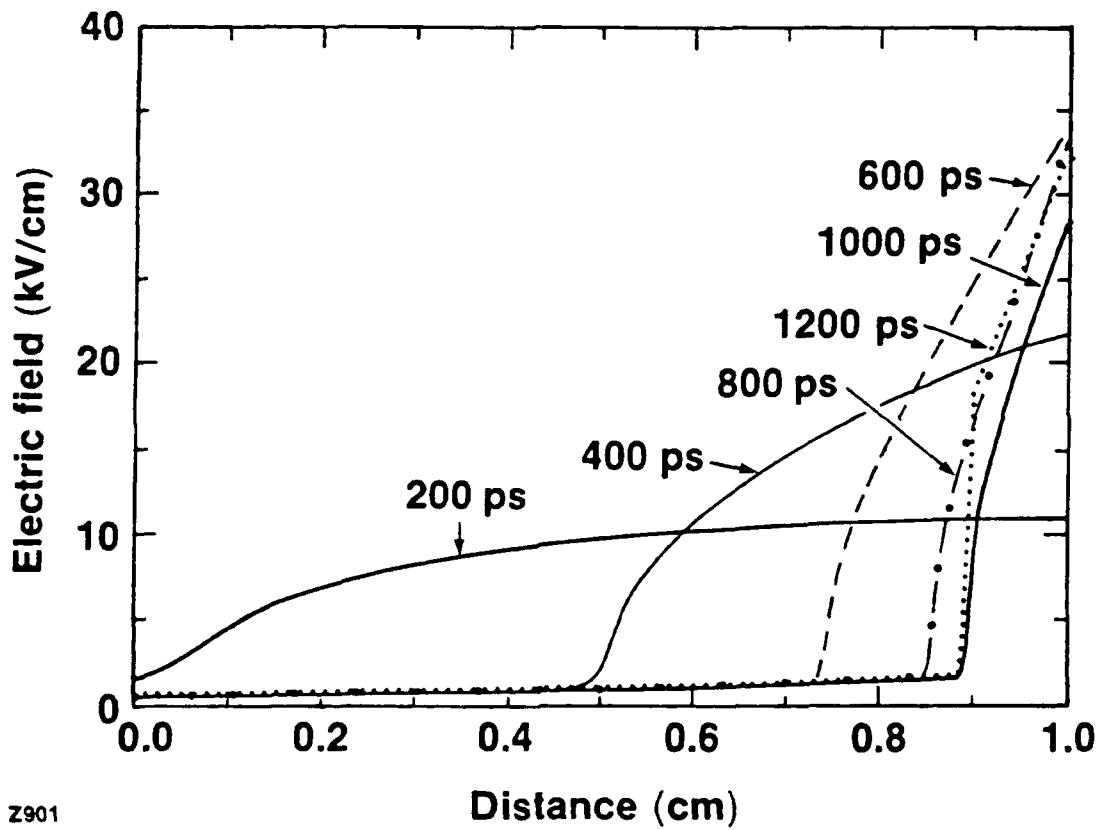
(b) Bulk Switches

The switching of the bulk GaAs switches with gridded electrodes was simulated. For these switches, illumination through the electrode grid was modelled by a propagating Gaussian optical pulse. The program parameters were: $l = 0.6$ cm; the conducting area, $A = 0.1$ cm; $\epsilon_r = 13.1$; and the absorption coefficient, $\sigma = 1.39$ cm. These parameters were chosen to represent the actual switches that were used in experiments. The value of A was the measured optical beam size. σ was measured at LLE for the samples provided. The applied optical pulse energy was $100 \mu\text{J}$ resulting in carrier densities of $\sim 10^{16}/\text{cm}^3$. The optical pulse variance was 200 ps.

A spatial profile of the electric field for an applied bias voltage of -9 kV is shown in Fig. 29 for illumination through the ground contact only. The electric field collapses in time from the ground contact to the negative high-voltage contact as the optical pulse propagates through the switch. The field is seen to "compress" as it collapses, forming a field peak at the contact opposite illumination. The field is compressed until, at 1200 ps, NDR effects take over. This sharpens the field gradient and rise in the field at the contact. Excellent qualitative agreement is obtained with the electric field profiles obtained experimentally for this illumination scheme, which is shown in Fig. 12(b).

Simultaneous illumination through both the ground and negative high-voltage electrode was also simulated. The calculated electric field profiles showed surprisingly uniform collapse. The simulated switching with two-side illumination was considerably more efficient than one-side illumination, with more complete field collapse and faster rise time, in agreement with experiment. The observed field peaking at the contacts (~ 1.2 times the bias field) is not reproduced in the two-side illumination modelling for ohmic contacts.

The observed decrease in the electro-optic switch efficiency is not recreated in the simulations. Simulations do not show significant field remaining across the switch after several nanoseconds. It is not possible to conclude, on the basis of this computer model,



Z901

Fig. 29 Electric field profiles during bulk switch operation with illumination through the ground contact.

that the observed decrease in electro-optic switch efficiency is due to negative differential resistance in the photoconductive switch.

The failure of the program to recreate exactly the observed field profiles is most probably due to the fact that the gridded electrode switches do not lend themselves completely to a one-dimensional analysis. To properly simulate the bulk switches with gridded electrodes, it would be necessary to model the conducting and nonconducting channels created by the electrode grid. There is probably considerable vertical structure that affects the field profile, as well. Simulation of these effects would require a much more advanced, three-dimensional model. Also, the field probe can only access the switch field at the switch surface and the surface field may not be a true measure of the internal field structure for switches with such considerable vertical structure.

2. Silicon switching

Silicon switch operation was also modeled. Si switches with the same physical dimensions as the planar GaAs switches, $l = 0.25$ cm, $w = 0.25$ cm, and $d = 0.05$ cm, were simulated with overhead illumination by Gaussian spatial profile laser pulses. Figure 30 shows calculated electric fields for -20 kV bias (80 kV/cm) and 150 ps FWHM, 1064 nm laser pulse with pulse energy of 100 μ J. τ was taken to be 73 μ s, a representative measured value, and ϵ_r was 11.9 [25]. The field collapse is quite uniform, with a direct relationship between the field profile and the density profile. This is typical of all the Si simulations run. Propagating domains, as in the GaAs simulations, are never seen, although simulations show high-field regions form in Si at the electrodes for tightly focused pump beams, similar to Fig. 7(b). Impact ionization acts to limit the field in these regions. The e-o images obtained with planar Si switches are in excellent qualitative agreement with profiles calculated using the experimental parameters.

The e-o measurements of the coaxial Si switch output waveform were compared to calculated waveforms. The comparison is not direct, as the model simulates a switch which

is a rectangular solid, not a cylinder as in the experiments. Also, the 1064-nm laser excitation pulse can only penetrate ~1 mm into the cylinder, so there is only a limited region of conduction whose shape is not easily defined. The cylindrical switch is a three-dimensional device, and is only approximated by a one-dimensional analysis. To model the cylindrical switch, a rectangular switch with a volume equivalent to the approximate conducting volume of the Si cylinder was used. Despite the limitations, the model accurately predicts some of the trends observed in the experimental waveforms. Figure 31 shows calculated waveforms for a Si switch biased at -10 kV. The degradation of switch rise time and efficiency with decreasing optical energy is seen in this figure. The model will also reproduce the observed voltage overshoot and risetime variation with bias for the appropriate input parameters. Simulation shows that impact ionization plays a significant role in switch behavior at high-bias fields, for the case of focused pump beams. In particular, simulation indicates that the observed increase in the coaxial switch efficiency at -19 kV bias, as opposed to -13 kV bias, is related to the onset of impact ionization in regions of the switch. The field compression induced by focusing leads to carrier gain by impact ionization. This reduces the final switch resistance at the higher bias, even though the total number of optically generated carriers is the same at either bias voltage.

V. BREAKDOWN INVESTIGATION

Two types of breakdown investigations were carried out. On bulk type photoconductive switches, the primary breakdown problem was along the contacts after the switch had been illuminated. The other breakdown problem was also optically initiated. GaAs surface switches were found to undergo a surface arcing event after they had been optically triggered. In both cases these optically triggered breakdown events were considered to be more detrimental than untriggered events because they happened under standard operating conditions and at lower fields. It does not make sense to have a switch

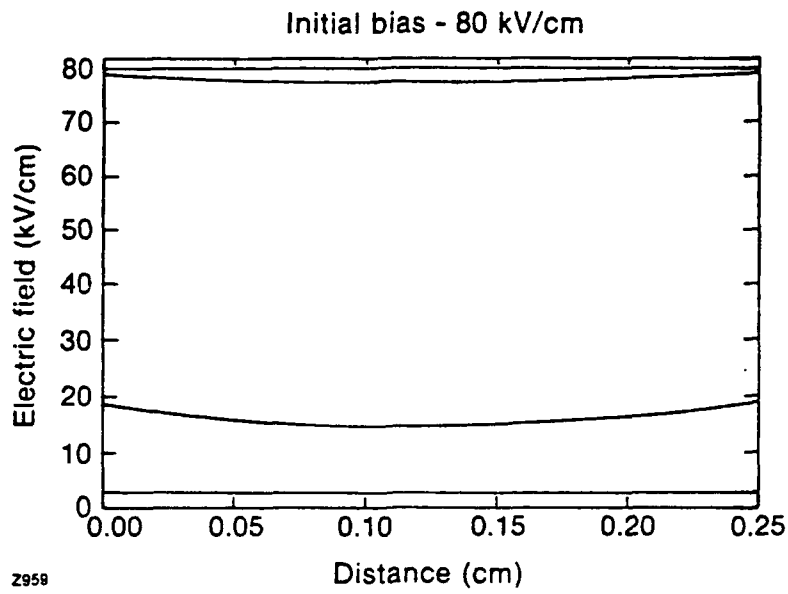


Fig. 30 Calculated electric field profiles for Si switch at bias of -20 kV. The field collapse is uniform. Switch recovery is not seen due to long recombination time of Si.

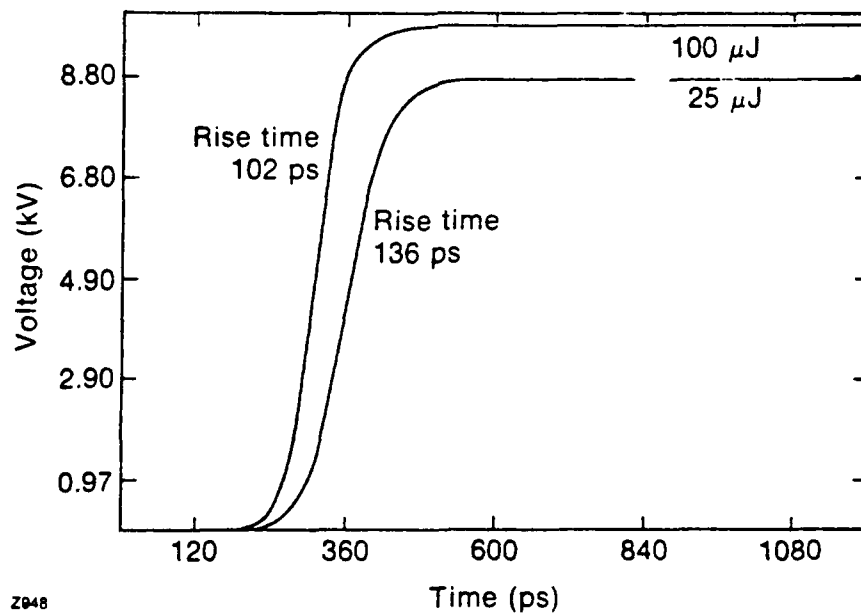


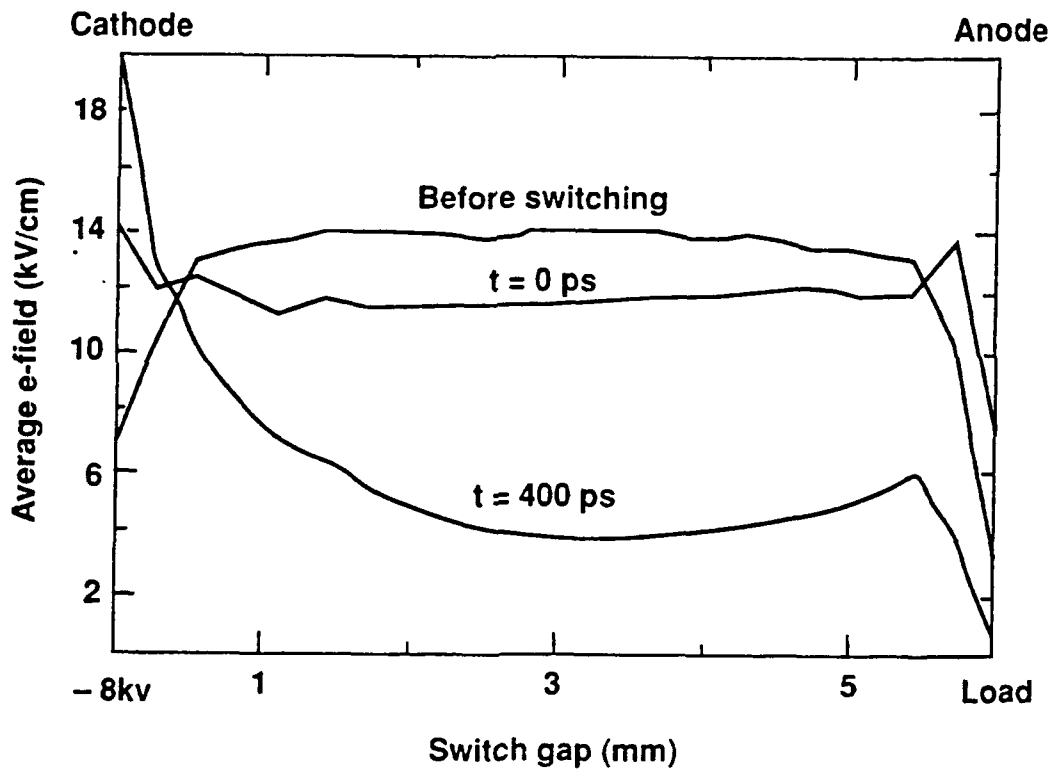
Fig. 31 Calculated Si switch output waveform at -10 kV bias. Note the decrease in switch efficiency and increase in switch risetime for decreasing optical energy.

that can withstand huge fields in the off state only to break down when it is actually switched.

The arcing on the bulk switches occurred from the gridded portion of the contacts to the solid outside ring that made contact to the external circuit. The arcing was confined to the cathode independent of whether the illumination was through the cathode, anode or both. The electro-optic images revealed very high field enhancements at the cathode. Figure 32 shows an average field across the width of the switch for a bulk switch illuminated from both sides. At 400 ps after the light pulse hits the switch, a field spike starts to build up at the cathode. This field spike is greater than the applied field of 14 kV/cm. If the field along the cathode is measured, it shows a very nonuniform structure. The variation is probably due to the gridded structure of the electrodes.

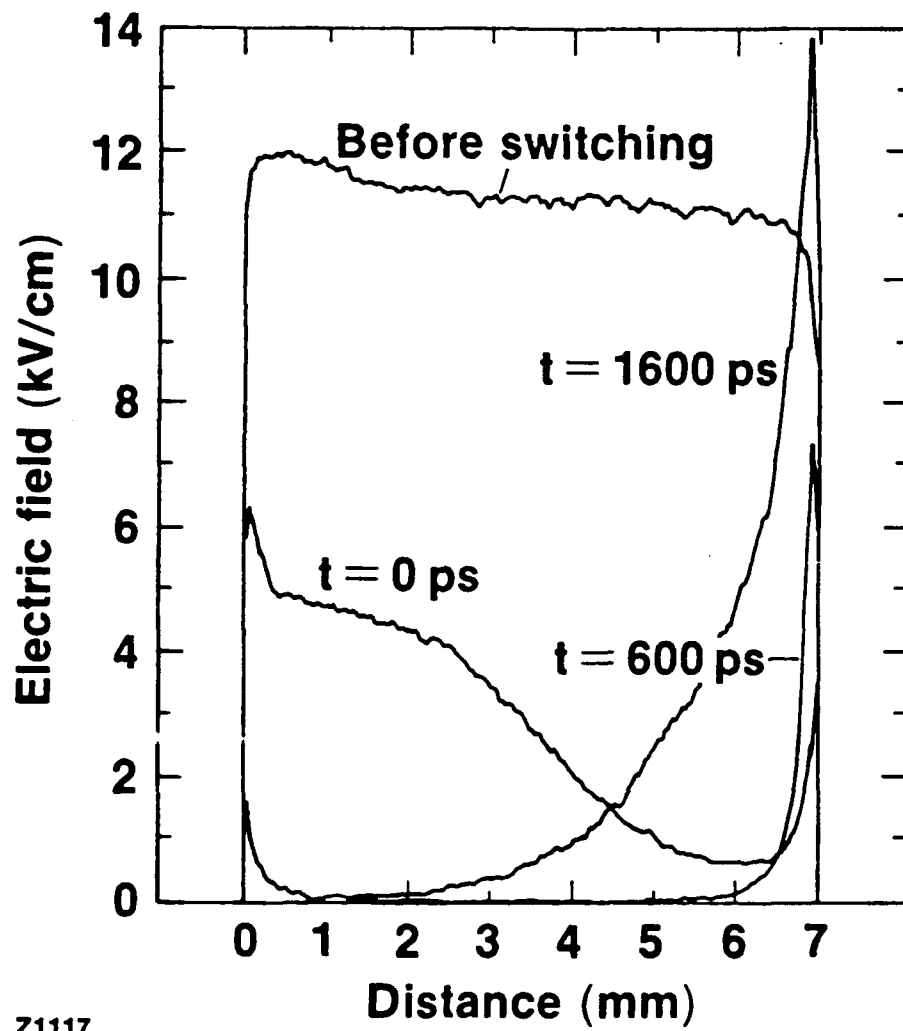
Computer simulations of the device in 1-D indicate that significant field enhancements can occur if the contacts are made to be completely noninjecting. This would be the case for the areas of the contact that are not covered with metalization. Without metalization there is no place to inject carriers from. To prevent breakdown along the contact, some method must be devised to improve injection and reduce the field at the contact.

Using this information, we worked with the U.S. Army ETDL in Fort Monmouth, NJ, to improve the switches. N-type contacts were fabricated on the GaAs by ion implanting Si at $10^{18}/\text{cc}$ to a depth of $0.1 \mu\text{m}$ under both the metalized and nonmetalized areas. As shown in Fig. 33, this dramatically reduced the field at the cathode. Breakdown no longer occurred at the cathode after this treatment. The n-type doping produced a forward-biased diode at the cathode. There continued to be a field enhancement at the anode although it was much less and did not seem to cause breakdown. Figure 34 shows the result of making the anode a forward-biased p-type contact by implanting it with Be. The doping profile was similar to the n-type contact. The field enhancements were reduced at both contacts in this case. Thus, as a result of this program, we are able to visualize the



Z1124

Fig. 32 The average field across a GaAs switch with intrinsic contact shows a field enhancement at the cathode.



Z1117

Fig. 33 A NIN contact reduces the field enhancement at the cathode.

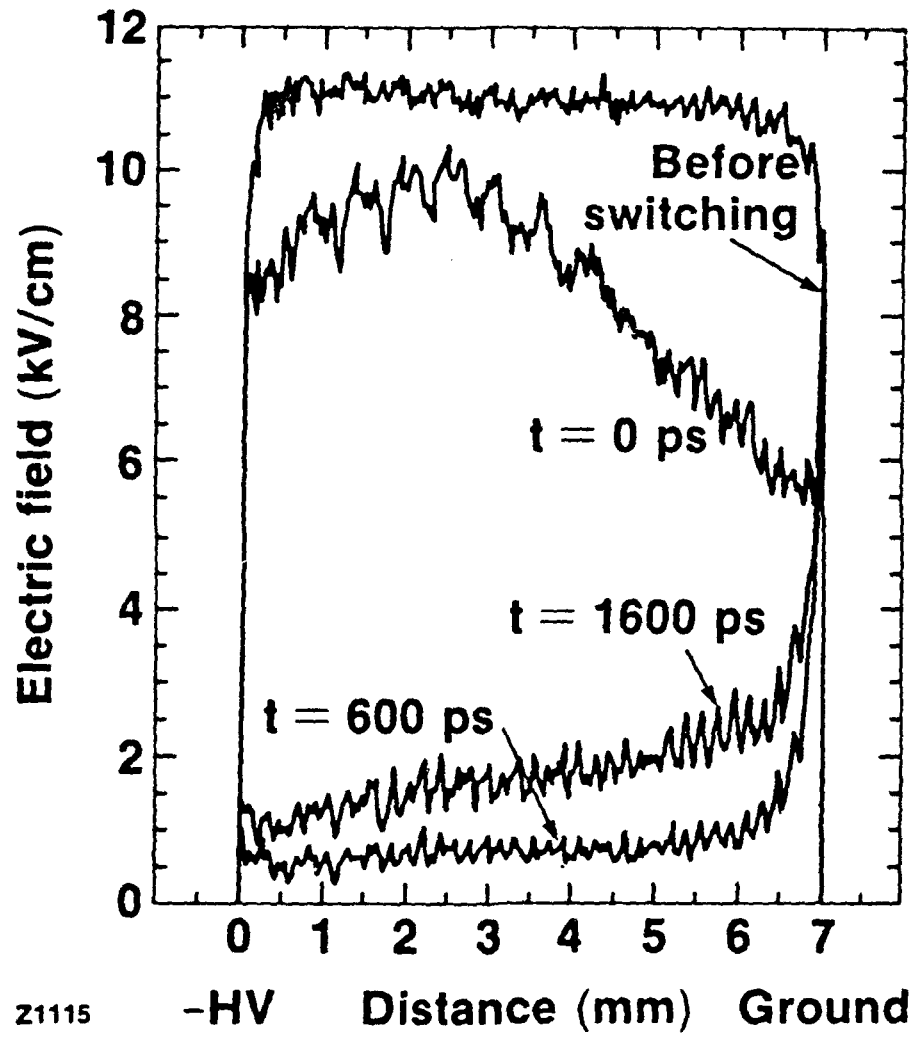


Fig. 34 A PIN contact reduces the field enhancement at both contacts.

field enhancements that occur at the contacts. These field enhancements cause serious degradation of the contacts. By turning the contacts into forward biased diodes, the problem can be eliminated.

To investigate surface GaAs switches, a setup was constructed as follows. The sample was biased with voltage pulse. At a time, t , where $t = -400$ ps to 200 ns after the voltage pulse, the field was probed with a green optical pulse. Two hundred picoseconds after the field was probed, a strong IR pulse was used to truncate the field and prevent the switch from arcing prematurely. This did not work. The switch arced whenever it was illuminated with the IR regardless of the time delay. When the IR was blocked, it never arced. It seems that the filamentation seen in earlier studies was a precursor to breakdown.

VI. SUMMARY

This research project has made contributions to the field of ultrafast, high-voltage, photoconductive switching, both in the area of experimental diagnostics and fundamental understanding.

The electro-optic probes developed here have made possible characterization of high-power switch operation on a picosecond time scale. The electro-optic measurement of the coaxial silicon switch output demonstrated the inadequacies of previous switch models and served as part of an experimental basis for our photoconductive switch model. The two-dimensional electro-optic imaging system can time-resolve the full spatial and temporal variations of the electric field over extended regions above semiconductor surfaces. This was not previously possible. The primary strength of this diagnostic is its ability to monitor events within the electrode gap itself. This is a distinct advantage over monitoring only the semiconductor device output waveform. Operating parameters can be measured with no electrical connection to the device circuit. Electric field profiles obtained with the imaging system have provided new and significant information about the behavior of GaAs photoconductive switches under high bias fields. In particular, some insight into the

mechanism for lock-on has been obtained. The formation of high-field domains at the cathode of planar GaAs switches during lock-on has been observed experimentally. This lends credence to lock-on theories that depend on high-field domain formation. Evidence for current channeling, which was unexpected, was obtained. Imaging of bulk GaAs switch operation showed electric field compression and variation with the applied bias field. The expected, relatively uninteresting, collapse of the electric field in silicon switches was also observed. This system can be used to image the field in other high-field devices, as well, providing a new diagnostic tool for the study of semiconductor devices. Extension of this work to integrated circuits could allow the characterization of devices without introducing connector or stripline effects. Integrated circuits, while low bias devices, require contacts to be closely spaced resulting in high fields between electrodes. Surface field maps of entire LSI circuits could be obtained with the electro-optic imaging system and be used to pinpoint possible breakdown points. Future work could center on improving the spatial resolution and sensitivity of the imaging system. Temporal resolution would be improved by using shorter optical pulses.

The computer-aided analysis of the photoconductive process agreed moderately well with the experimental data. The one-dimensional model, although simplistic, accurately simulates pulsed-power switching. Simulation data indicates that negative differential resistance is most probably the cause of the nonlinear behavior in GaAs. Although lock-on effects are not observed in the simulation data, the computer model can be used as an aid in determining the lock-on mechanism. Ionization of traps, for example, could be included in the model and suspect traps could be verified by experiment. Different recombination formulae could also be tried. The program could be modified to be applicable to a wider variety of semiconductor devices by using the appropriate numerical technique to deal with carrier diffusion. Although this was unnecessary for the simulation of high-voltage switches this would allow simulation of low-bias devices.

VII. REFERENCES

- [1] P. le Fur and D. H. Auston, "A Kilovolt Picosecond Optoelectronic Switch and Pockels Cell," *Appl. Phys. Lett.* **28**, 21-23 (1976).
- [2] G. Mourou and W. Knox, "High Power Switching with Picosecond Precision," *Appl. Phys. Lett.* **35**, 492 (1979).
- [3] W. R. Donaldson, "Ultrafast High Power Switching: Techniques and Applications," Proceedings, ELECTRO/89, New York, April, 1989.
- [4] W. C. Nunnally and R. B. Hammond, "80-MW Photoconductor Power Switch," *Appl. Phys. Lett.* **44**, 980 (1984).
- [5] G. Mourou, J. Bunkenburg, and W. Seka, "Electro-Optic Prepulse Suppression for Laser Fusion Systems," *Opt. Commun.* **34**, 252 (1980).
- [6] J. Agostinelli, G. Mourou, and C. W. Gabel, "Active Pulse Shaping in the Picosecond Domain," *Appl. Phys. Lett.* **35**, 731 (1979).
- [7] M. Stavola, J. Agostinelli, and M. Sceats, "Ultrafast Pulse Shaping with a Travelling Wave Kerr Cell and Picosecond Rise Time Electrical Pulse," *Appl. Opt.* **18**, 4101 (1979).
- [8] G. Mourou and W. Knox, "A Picosecond Jitter Streak Camera," *Appl. Phys. Lett.* **36**, 623 (1980).
- [9] G. Mourou, C. V. Stancampiano, A. Antonetti, and A. Orzag, "Picosecond Microwave Pulses Generated with a Subpicosecond Laser-Driven Semiconductor Switch," *Appl. Phys. Lett.* **39**, 295 (1981).
- [10] W. Margulis, W. Sibbett, and J. R. Taylor, "Active Mode-Locking of Lasers Using GaAs and GaP Picosecond Switches," *Opt. Commun.* **35**, 153 (1980).
- [11] C. Bamber, W. Donaldson, T. Juhasz, L. Kingsley, and A. C. Melissinos, "Radial Compression of Picosecond Electrical Pulses," *Part. Accel.* **23**, 255 (1988).
- [12] J. A. Valdmanis, G. Mourou, and C. W. Gabel, "Subpicosecond Electrical Sampling," *IEEE J. Quantum Electron.* **QE-19**, 664 (1983).
- [13] L. E. Kingsley and W. R. Donaldson, "Electro-Optic Surface Field Imaging System," *Digest of Technical Papers*, 7th IEEE Pulsed Power Conf., edited by R. White and B. H. Bernstein (IEEE, New York, 1989), pp. 376-379.
- [14] L. E. Kingsley and W. R. Donaldson, "Two-Dimensional Electro-Optic Imaging," *Conference on Lasers and Electro-optics Technical Digest Series 1989, Vol. 11* (Optical Society of America, Washington, D.C., 1989), pp. 112-114.
- [15] L. E. Kingsley and W. R. Donaldson, "Electro-Optic Imaging of Surface Electric Fields in High-Power Photoconductive Switches," *IEEE Trans. Electron. Devices*, **ED-37** (12) 2449 (1990).

- [16] W. R. Donaldson, L. E. Kingsley, M. Weiner, A. Kim, and R. Zeto, "Electro-optic Imaging of the Internal Fields in a GaAs Photoconductive Switch," *J. Appl. Phys.* **68** (12) 6453 (1990).
- [17] L. E. Kingsley and W. R. Donaldson, "Optical Probing of Semiconductor Carrier Dynamics," *Conference on Lasers and Electro-optics Technical Digest Series 1990, Vol. 7* (Optical Society of America, Washington, D.C., 1990), p. 150.
- [18] L. Bovino, T. Burke, R. Youmans, M. Weiner, and J. Carter, "Recent Advances in Optically Controlled Bulk Semiconductor Switches," *Digest of Technical Papers, 5th IEEE Pulse Power Conf.*, edited by P. J. Turchi and M. F. Rose (IEEE, New York, NY, 1985), p. 242-245.
- [19] W. Donaldson and L. Kingsley, "Optical Probing of Field Dependent Effects in GaAs Photoconductive Switches," *SPIE Symposium on Laser Science & Optical Applications, OE/Boston '90, 4-9 November 1990* (proceedings to be published).
- [20] G. M. Loubriel, M. W. O'Malley, and F. J. Zutavern, "Toward Pulsed Power Uses for Photoconductive Switches: Closing Switches," *Digest of Technical Papers, 6th IEEE Pulsed Power Conf.*, edited by P. J. Turchi and B. H. Bernstein (IEEE, New York, 1987), pp. 145-148.
- [21] F. J. Zutavern, G. M. Loubriel, and M. W. O'Malley, "Recent Developments in Opening Photoconductive Semiconductor Switches," *Digest of Technical Papers, 6th IEEE Pulsed Power Conf.*, edited by P. J. Turchi and B. H. Bernstein (IEEE, New York, 1987), pp. 577-580.
- [22] F. J. Zutavern, G. M. Loubriel, R. B. McKenzie, M. W. O'Malley, R. A. Hamil, L. P. Schanwald, and H. P. Hjalmarson, "Photoconductive Semiconductor Switch (PCSS) Recovery," *7th IEEE Pulsed Power Conf.*, edited by R. White and B. H. Bernstein (IEEE, New York, 1989), pp. 412-417.
- [23] G. M. Loubriel, F. J. Zutavern, H. P. Hjalmarson, and M. W. O'Malley, "Closing Photoconductive Semiconductor Switches," *Digest of Technical Papers, 7th IEEE Pulsed Power Conf.*, edited by R. White and B. H. Bernstein (IEEE, New York, 1989), pp. 365-367.
- [24] H. Kroemer, "Theory of the Gunn Effect," *Proc. IEEE* **52**, 1736 (1964).
- [25] S. M. Sze, *Physics of Semiconductor Devices*, 2nd ed. (John Wiley and Sons, New York, 1981), p. 652.
- [26] *Ibid*, Chapter 11, pp. 637-678.
- [27] R. Pastore and M. Weiner, "RF Oscillations in Optically Activated Semi-Insulating GaAs," *Digest of Technical Papers, 7th IEEE Pulsed Power Conf.*, edited by R. White and B. H. Bernstein (IEEE, New York, 1989), pp. 872.
- [28] K. Meyer, "Study of Picosecond Electron Transport in GaAs Using Transient Photoconductivity and Transient Absorption Spectroscopy," Thesis (Ph.D.), University of Rochester, Dept. of Physics and Astronomy (1988).
- [29] A. E. Iverson and D. L. Smith, "Mathematical Modeling of Photoconductor Transient Response," *IEEE Trans. Electron. Devices* **ED-34** (10), 2098 (1987).

- [30] A. E. Iverson, D. L. Smith, N. G. Paultier, and R. B. Hammond, "Transient Photoconductive Response of InP:Fe," *J. Appl. Phys.* **61** (1), 234 (1987).
- [31] A. E. Iverson, "The Mathematical Modeling of Photoconductive Power Switches," *Trans. Soc. Comp. Simul.* **5** (3), 175 (1988).
- [32] M. Weiner, L. Bovino, R. Youmans, and T. Burke, "Modeling of the Optically Controlled Semiconductor Switch," *J. Appl. Phys.* **60** (2), 823 (1986).
- [33] W. T. White, C. G. Dease, M. D. Pocha, and G. H. Khanaka, "Modeling GaAs High-Voltage Subnanosecond Photoconductive Switches in One Spatial Dimension," *IEEE Trans. Electron. Devices* **ED-37** (12), 2532 (1990).
- [34] E. Sano and T. Shibata, "Fullwave Analysis of Picosecond Photoconductive Switches," *IEEE J. Quantum Electron.* **26** (2), 372 (1990).
- [35] S. M. Sze, *Physics of Semiconductor Devices*, 2nd ed. (John Wiley and Sons, New York, 1981), pp. 45-49.
- [36] K. Horio, T. Ikoma, and H. Yanai, "Computer-Aided Analysis of GaAs n-i-n Structures with a Heavily Compensated Layer," *IEEE Trans. Electron. Devices* **ED-33** (9), 1242 (1986).
- [37] Sze op. cit., p. 325.
- [38] P. J. Roache, *Computational Fluid Dynamics*, (Hermosa, Albuquerque, New Mexico, 1982), p. 20.
- [39] Ibid, p. 72
- [40] Ibid, p. 345-349.
- [41] W. H. Press, *Numerical Recipes*, (Cambridge University Press, Cambridge, New York, Melbourne, 1986), pp. 626-627.
- [42] D. L. Scharfetter and H. K. Gummel, "Large-Signal Analysis of a Silicon Read Diode Oscillator," *IEEE Trans. Electron. Devices* **ED-16** (1), 64 (1969).
- [43] Sze, op. cit., pp. 850-851.
- [44] M. Ohtomo, "Nucleation of High-Field Domains in n-GaAs," *Jpn. J. Appl. Phys.* **7** (11), 1368 (1968).
- [45] J. S. Heeks, "Some Properties of the Moving High-field Domain in Gunn Devices," *IEEE Trans. Electron. Devices* **ED-13** (1), 68 (1966).